



Cite this: DOI: 10.1039/d0ee01457e

## Assessing the viability of K-Mo<sub>2</sub>C for reverse water–gas shift scale-up: molecular to laboratory to pilot scale†

Mitchell Juneau,<sup>a</sup> Madeline Vonglis,<sup>a</sup> Joseph Hartvigsen,<sup>b</sup> Lyman Frost,<sup>b</sup> Dylan Bayerl,<sup>c</sup> Mudit Dixit,<sup>c</sup> Giannis Mpourmpakis,<sup>c</sup> James R. Morse,<sup>d</sup> Jeffrey W. Baldwin,<sup>e</sup> Heather D. Willauer<sup>\*d</sup> and Marc D. Porosoff<sup>\*a</sup>

Conversion of CO<sub>2</sub> to value-added chemicals and fuels is a potentially valuable route for renewable energy storage and a future CO<sub>2</sub>-neutral economy. The first step is CO<sub>2</sub> conversion to CO via the reverse water–gas shift (RWGS) reaction. Effluent CO can then be hydrogenated to chemicals and fuels via Fischer–Tropsch (FT) synthesis over a tandem catalyst or within a second reactor. To implement this process on an industrial scale, low-cost, scalable and highly-selective catalysts are required, prompting investigations into materials that meet these design constraints. Potassium-promoted molybdenum carbide supported on gamma alumina (K-Mo<sub>2</sub>C/γ-Al<sub>2</sub>O<sub>3</sub>) has recently been shown to be a highly active and selective RWGS catalyst in the laboratory, prompting us to investigate the viability of K-Mo<sub>2</sub>C/γ-Al<sub>2</sub>O<sub>3</sub> for scale-up. In this report, laboratory-scale (~100 mg catalyst) reactor studies are extended to the pilot-scale (~1 kg catalyst), and viability for scale-up is tested further with density functional theory (DFT) calculations, detailed characterization and reactor experiments under a range of temperatures (300–600 °C) and flow conditions. The pilot-scale experiments illustrate K-Mo<sub>2</sub>C/γ-Al<sub>2</sub>O<sub>3</sub> is a highly active and selective catalyst (44% CO<sub>2</sub> conversion, 98%+ CO selectivity at GHSV = 1.7 L kg<sup>-1</sup> s<sup>-1</sup> and T = 450 °C) that exhibits no signs of deactivation for over 10 days on stream. Together, experiments across the molecular, laboratory and pilot scales demonstrate that K-Mo<sub>2</sub>C/γ-Al<sub>2</sub>O<sub>3</sub> is an economically-viable RWGS catalyst with promising future applications in the US Naval Research Laboratory's seawater-to-fuel process, downstream methanol synthesis and FT.

Received 8th May 2020,  
Accepted 7th July 2020

DOI: 10.1039/d0ee01457e

rsc.li/ees

### Broader context

Conversion of CO<sub>2</sub> into chemicals and fuels is a potentially valuable route for renewable energy storage and a future CO<sub>2</sub>-neutral economy. The first step of a thermally-driven route for CO<sub>2</sub> conversion is typically CO production *via* the reverse water–gas shift (RWGS) reaction. Depending on the application, CO is subsequently hydrogenated into methanol, light olefins or fuels. To develop an industrially deployable catalyst for RWGS, it is necessary to synthesize a low-cost and scalable catalyst that demonstrates high performance without deactivation. The current work contains a unique group of experiments that move us toward solving this challenge, by demonstrating K-Mo<sub>2</sub>C/γ-Al<sub>2</sub>O<sub>3</sub> outperforms all other reverse water–gas shift catalysts reported in literature under similar conditions. The broad scope of our study is the first of its kind that correlates density functional theory calculations with laboratory-scale measurements (~100 mg catalyst) and pilot-scale reactor studies (1 kg catalyst), to assess the scale-up viability of K-Mo<sub>2</sub>C/γ-Al<sub>2</sub>O<sub>3</sub>. The catalyst under investigation is currently being deployed by the US Naval Research Laboratory as part of a project to provide fuel at sea. The pilot-scale system is capable of producing up to four liters of liquid hydrocarbon fuel per day from CO<sub>2</sub> extracted from seawater.

<sup>a</sup> Department of Chemical Engineering, University of Rochester, Rochester, NY, 14627, USA. E-mail: marc.porosoff@rochester.edu

<sup>b</sup> OxEon Energy, LLC, North Salt Lake, UT, 84054, USA

<sup>c</sup> Department of Chemical and Petroleum Engineering, University of Pittsburgh, Pittsburgh, PA, 15261, USA

<sup>d</sup> Materials Science and Technology Division, Naval Research Laboratory, Washington, DC, 20375, USA. E-mail: heather.willauer@nrl.navy.mil

<sup>e</sup> Acoustics Division, Naval Research Laboratory, Washington, DC, 20375, USA

† Electronic supplementary information (ESI) available: Further details on pilot-scale synthesis and characterization, along with laboratory-scale performance and characterization information and DFT structural configurations. See DOI: 10.1039/d0ee01457e

### Introduction

Consumption of fossil fuels has led to increasing atmospheric and oceanic carbon dioxide concentrations, which are negatively impacting the global environment due to their role in climate change and ocean acidification. In efforts to counteract these negative effects, significant research has been undertaken to develop technologies capable of capturing and converting CO<sub>2</sub> into commodity chemicals and fungible fuels.<sup>1–6</sup> In recent years,

research into direct air capture of CO<sub>2</sub> has expanded, a necessary step to reduce the concentration of atmospheric CO<sub>2</sub>.<sup>7</sup> In a future CO<sub>2</sub>-based cyclical economy, the captured CO<sub>2</sub> could be directly input into a CO<sub>2</sub> hydrogenation process to produce chemicals and fuels from CO<sub>2</sub> and renewable H<sub>2</sub>.

Currently, the field of CO<sub>2</sub> capture and conversion is experiencing rapid growth as CO<sub>2</sub> is both an abundant and inexpensive C<sub>1</sub> feedstock that can be used as a platform chemical for renewable energy storage.<sup>8</sup> However, implementation of pilot-scale CO<sub>2</sub> conversion processes is limited by the specific economics of the region. For example, Canada and Iceland have both undertaken CO<sub>2</sub> capture and conversion efforts to produce synthetic fuels and methanol, respectively.<sup>9,10</sup> Within pilot-scale CO<sub>2</sub> conversion processes, CO<sub>2</sub> hydrogenation is typically conducted thermochemically *via* modified Fischer-Tropsch (FT) synthesis, with CO<sub>2</sub> substituted for the CO reactant (CO<sub>2</sub>-FT).<sup>11–15</sup> In CO<sub>2</sub>-FT, CO<sub>2</sub> is first converted to CO *via* endothermic reverse water-gas shift (RWGS, scheme 1), followed by subsequent hydrogenation of CO to hydrocarbon products *via* exothermic FT. Therefore, to achieve high yield toward the desired hydrocarbon products (C<sub>6+</sub>), the equilibrium-limited RWGS reaction is typically operated at high temperatures (>600 °C) to achieve high CO<sub>2</sub> conversion and prevent CO<sub>2</sub> from entering the downstream FT reactor

where it can be converted to undesired CH<sub>4</sub> *via* the Sabatier reaction.<sup>16</sup>

Achieving high selectivity toward desirable CO for downstream FT at more moderate temperatures (~450 °C) with lower energy input is difficult because the methanation and Sabatier side reactions (schemes 2 and 3) are highly thermodynamically favorable under these lower temperature RWGS conditions.<sup>17</sup>



One option for achieving high performance during RWGS is to use well-established forward water-gas shift catalysts for the reverse reaction.<sup>18,19</sup> As shown in Fig. 1 (sample calculations are included in the ESI†), the low temperature industrial catalyst (Cu-ZnO/Al<sub>2</sub>O<sub>3</sub>) is a top performing catalyst at 300 °C with a CO space-time yield (STY) of 80.2 μmol CO g<sub>cat</sub><sup>-1</sup> s<sup>-1</sup> and CO selectivity of 92.6%. However, the high temperature industrial catalyst (FeCrO<sub>x</sub>) performs poorly at 450 °C with a CO STY of 21.5 μmol CO g<sub>cat</sub><sup>-1</sup> s<sup>-1</sup> because of a low CO selectivity of 48.6%.

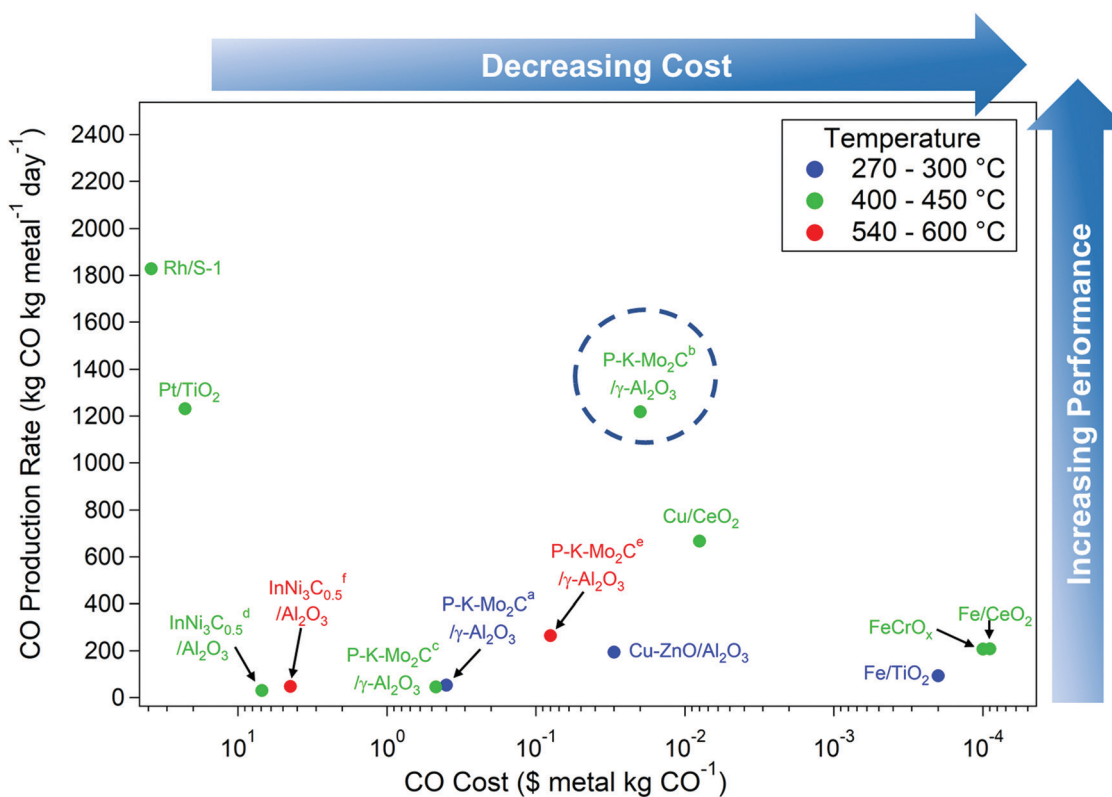


Fig. 1 Metrics for comparing state-of-the-art RWGS catalysts. CO production rate (kg CO kg metal<sup>-1</sup> day<sup>-1</sup>) is plotted versus CO cost (\$ metal kg CO<sup>-1</sup>) for selected catalysts. Sample calculations for CO production rate and CO cost are included in the ESI† and specific reaction conditions with detailed performance for each catalyst are found in Table 4 (Discussion section). P-K-Mo<sub>2</sub>C/γ-Al<sub>2</sub>O<sub>3</sub> reaction conditions are as follows: (a) 300 °C, 2.1 MPa, 36.7 L kg<sup>-1</sup> s<sup>-1</sup>; (b) 450 °C, 2.1 MPa, 36.7 L kg<sup>-1</sup> s<sup>-1</sup>; (c) 450 °C, 0.1 MPa, 1.8 L kg<sup>-1</sup> s<sup>-1</sup>; (e) 600 °C, 2.1 MPa, 3.7 L kg<sup>-1</sup> s<sup>-1</sup>. InNi<sub>3</sub>C<sub>0.5</sub>/Al<sub>2</sub>O<sub>3</sub> reaction conditions are as follows: (d) 420 °C, 1 MPa, 1.7 L kg<sup>-1</sup> s<sup>-1</sup>; (f) 540 °C, 1 MPa, 1.7 L kg<sup>-1</sup> s<sup>-1</sup>.

Precious metal-based catalysts are also promising candidates for RWGS.<sup>20,21</sup> Recent studies show that for RWGS over Rh supported on silicalite-1 (S-1) at 450 °C and Pt supported on TiO<sub>2</sub> at 400 °C result in high CO selectivities of 71.3% and 100% and CO STYs of 3.0 μmol CO g<sub>cat</sub><sup>-1</sup> s<sup>-1</sup> and 5.0 μmol CO g<sub>cat</sub><sup>-1</sup> s<sup>-1</sup>, respectively.<sup>22,23</sup> However, Pt-based catalysts exhibit deactivation and decreased selectivity toward CO with increased time-on-stream, limiting their applicability in a scaled-up process.<sup>24</sup> Additionally, the high material costs of Rh and Pt result in a high cost of CO when compared to other top-performing transition metal catalysts, as shown in Fig. 1. For example, at 400 °C with a 4 : 1 H<sub>2</sub> : CO<sub>2</sub> ratio, Fe and Cu supported on CeO<sub>2</sub> exhibit reasonable CO<sub>2</sub> conversions of 8.1% and 31.3%, both with 100% CO selectivities at atmospheric pressure and a moderately high GHSV (gas hourly space velocity) of 16.7 L kg<sup>-1</sup> s<sup>-1</sup>, resulting in a very low cost of CO when compared to the precious metal catalysts.<sup>25</sup>

Other low-cost alternatives to precious metal catalysts are transition metal carbides (TMCs), which exhibit comparable activity and selectivity to their precious metal counterparts for many reactions, including RWGS.<sup>26</sup> These observed experimental trends have been corroborated with density functional theory (DFT) calculations, indicating that incorporation of carbon into the transition metal lattice attenuates the electronic properties of the catalyst, and in turn, adsorption of the reactants, intermediates and products.<sup>27–29</sup> Detailed investigations into TMCs for RWGS have shown that unsupported Mo<sub>2</sub>C can outperform commonly used Pt and Pd-based bimetallic catalysts,<sup>30–32</sup> while supported Mo<sub>2</sub>C and WC are also active and selective for producing CO *via* RWGS.<sup>33,34</sup> The higher activity observed over TMCs is a result of CO<sub>2</sub> activation occurring *via* direct C=O bond scission, without formation of any carbonates or formates, the typical intermediates observed over precious metal-based catalysts.<sup>35</sup>

To further improve the catalytic properties of TMCs for RWGS, alkali metals are incorporated into the catalyst matrix as low-cost promoters to attenuate the electronic and structural properties of the TMC,<sup>27,34,36</sup> resulting in increased CO<sub>2</sub> binding energy and a decreased energy barrier for CO<sub>2</sub> dissociation.<sup>37–39</sup> These results are confirmed in reactor studies of potassium promoted Mo<sub>2</sub>C and WC supported on γ-Al<sub>2</sub>O<sub>3</sub>, which both show an increase in CO selectivity and stability during RWGS.<sup>40,41</sup> The favorable catalytic properties of alkali-promoted TMCs along with their low-cost and facile synthesis suggest that these catalysts, and K-Mo<sub>2</sub>C in particular, have high potential for scale-up.

When evaluating a catalyst for scale-up, it is important to synthesize the catalyst with a scalable synthesis method, such as wet impregnation, using low-cost materials. Once synthesized, the catalyst must exhibit high stability over thousands of hours on stream and be easily regenerable to maximize catalyst lifetime.<sup>42,43</sup> It is also necessary to consider the reactor operating conditions, CO purity and cost of CO. Investigations are performed at varying temperatures and gas hourly space velocities, requiring metrics to better describe the scalability of top-performing laboratory-scale RWGS catalysts. As shown in Fig. 1, with specific conditions and detailed performance of additional

catalysts found in Table 4 (Discussion section), we have demonstrated in the current work that the low-cost and highly active catalyst, K-Mo<sub>2</sub>C/γ-Al<sub>2</sub>O<sub>3</sub> is overall the top performing catalyst for RWGS when accounting for CO purity, CO STY and the cost of the catalyst per kg of CO produced. To better understand the high performance of K-Mo<sub>2</sub>C/γ-Al<sub>2</sub>O<sub>3</sub> and applicability in an industrial process, we have performed a detailed study of the catalyst performance across different scales, from molecular to laboratory to pilot.

In this paper, laboratory and pilot-scale reactor experiments are combined with DFT calculations and catalyst characterization using X-ray diffraction (XRD), X-ray photoelectron spectroscopy (XPS) and pulse chemisorption to show that K-Mo<sub>2</sub>C/γ-Al<sub>2</sub>O<sub>3</sub> is a highly active, selective and stable RWGS catalyst. The pilot-scale catalyst, P-K-Mo<sub>2</sub>C/γ-Al<sub>2</sub>O<sub>3</sub>, is synthesized on an industrial γ-Al<sub>2</sub>O<sub>3</sub> trilobe support, and high performance is first demonstrated in the laboratory with CO selectivity greater than 99% over 100 h+ on stream at 450 °C. At very high temperature (600 °C), CH<sub>4</sub> becomes the primary product, likely because of coking and oxidation of the active phase.

Extending the results of P-K-Mo<sub>2</sub>C/γ-Al<sub>2</sub>O<sub>3</sub> to the kilogram scale in a pilot reactor at OxEon Energy (Fig. 2) at 450 °C and a GHSV of 1.7 L kg<sup>-1</sup> s<sup>-1</sup>, results in CO selectivities >98% with no signs of deactivation after 10 days on stream. The combined laboratory and pilot-scale experiments clearly demonstrate K-Mo<sub>2</sub>C/γ-Al<sub>2</sub>O<sub>3</sub> is a low-cost, high performance RWGS catalyst, suitable for scale-up and integration into high throughput processes to convert CO<sub>2</sub> into value-added chemicals and fuels.

## Experimental

### Laboratory-scale (L-K-Mo<sub>2</sub>C/γ-Al<sub>2</sub>O<sub>3</sub>) catalyst preparation

The laboratory-scale K-Mo<sub>2</sub>C was synthesized on γ-Al<sub>2</sub>O<sub>3</sub> (Alfa Aesar, 99.97% pure, 3 micron APS powder) *via* incipient wetness impregnation of potassium nitrate (Alfa Aesar, 99.995% pure) and



Fig. 2 Pilot-scale reactor with (left) and without (right) insulation, where band heaters are visible and wrapped around the reactor. The full piping and instrumentation diagram is available in Fig. S6 of the ESI.†

ammonium molybdate (para) tetrahydrate (Alfa Aesar, 99% pure) with a target of 2 wt% K and 20 wt% Mo loading for a target molar ratio of 1/4/15 K/Mo/ $\gamma$ -Al<sub>2</sub>O<sub>3</sub>. The catalysts were dried at 35 °C, calcined at 350 °C with 5 °C min<sup>-1</sup> ramp rate, and then carburized at 600 °C in a 21% CH<sub>4</sub>/H<sub>2</sub> mixture for 5 h. After carburization, the catalyst was passivated in a 1% O<sub>2</sub>/N<sub>2</sub> gas mixture.

### Pilot-scale (P-K-Mo<sub>2</sub>C/ $\gamma$ -Al<sub>2</sub>O<sub>3</sub>) catalyst preparation

The pilot-scale K-Mo<sub>2</sub>C was synthesized on trilobe  $\gamma$ -Al<sub>2</sub>O<sub>3</sub> via 3-step incipient wetness impregnation with target molar ratios of 1/4/15 K/Mo/ $\gamma$ -Al<sub>2</sub>O<sub>3</sub>, using the same potassium and molybdenum precursors as the laboratory-scale catalyst. After drying, the catalyst was calcined for 6 h at 350 °C, followed by carburization at 660 °C for 4 h in a 21% CH<sub>4</sub> in H<sub>2</sub> gas mixture. The higher carburization temperature was necessary because of a lack of carbide phase observed after 600 °C carburization. The catalyst was then passivated in 5% O<sub>2</sub> in N<sub>2</sub>. To synthesize P-K-Mo<sub>2</sub>C under laboratory-scale conditions (LC-P-Mo<sub>2</sub>C), after carburization the P-K-Mo<sub>2</sub>C catalyst was oxidized at 350 °C under static air conditions in a muffle furnace and then recarburized and passivated according to the above laboratory-scale (L-K-Mo<sub>2</sub>C/ $\gamma$ -Al<sub>2</sub>O<sub>3</sub>) catalyst preparation. Additional details of the pilot-scale catalyst synthesis can be found in Fig. S1–S5, Tables S1 and S2 of the ESI.<sup>†</sup>

### X-ray diffraction (XRD)

XRD patterns of the catalysts were recorded on a Malvern Panalytical multi-purpose diffractometer using CuK $\alpha$  radiation operated at 40 kV and 30 mA over the range of 2 $\theta$  = 5°–70° with a 0.03° step size and 0.5 s per step at room temperature. Powder diffraction patterns (PDFs) used for peak assignment: MoO<sub>2</sub> [PDF: 00-032-0671], Mo<sub>2</sub>C [PDF: 00-035-0787], MoC [PDF: 00-045-1015] and  $\gamma$ -Al<sub>2</sub>O<sub>3</sub> [PDF: 00-050-0741].

### Laboratory-scale reactor studies

To measure the catalytic performance for RWGS, laboratory-scale flow reactor studies were performed with 50 mg to 1 g of catalyst, depending on the desired GHSV, packed in a  $\frac{1}{2}$ " diameter, 12" long, stainless steel reactor and reduced under 40 sccm H<sub>2</sub> for 2 h at 300 °C and 0.34 MPa. After reduction, the reactor was isolated and the bypass pressurized to 2.1 MPa with specific gas flow rates and catalyst loadings to reach the desired GHSV.

Unless otherwise noted, reactions were run for 12 h at 300 °C, 450 °C and 600 °C at 2.1 MPa with a 3:1 H<sub>2</sub>:CO<sub>2</sub> ratio. For laboratory-scale RWGS reaction experiments, reactant flow rates of 30 sccm of H<sub>2</sub>, 10 sccm of CO<sub>2</sub> and 5 sccm of Ar as an internal standard were typically used, but for time-on-stream studies, flow rates were increased to 75 sccm of H<sub>2</sub>, 25 sccm of CO<sub>2</sub> and 10 sccm of Ar to maintain the H<sub>2</sub>:CO<sub>2</sub> ratio at 3:1. Concentrations of reactants and products were analyzed by an in-line Agilent Technologies 7890B gas chromatograph equipped with a flame ionization detector (FID) and a thermal conductivity detector (TCD). The concentration of each gas-phase species was calibrated by correlating the peak area of the pure compound to its concentration in a calibration gas standard.

The industrial FeCrO<sub>x</sub> used as comparison for laboratory-scale reactor studies was an Alfa Aesar iron-chrome based high temperature water–gas shift catalyst, HiFUEL® W210. The industrial Cu-ZnO/Al<sub>2</sub>O<sub>3</sub> catalyst was an Alfa Aesar copper-based low temperature water–gas shift catalyst, HiFUEL® W220.

### Pilot-scale reactor studies

All pilot-scale experiments were conducted by OxEon Energy LLC. The OxEon Energy pilot gas-to-liquids (GTL) system included a natural gas reformer, syngas compression and storage, and a Fischer-Tropsch reactor with cooling loop and recycle. For testing the P-K-Mo<sub>2</sub>C/ $\gamma$ -Al<sub>2</sub>O<sub>3</sub> catalyst, the syngas compressor was fed by a bulk CO<sub>2</sub> tank and dual hydrogen tank clusters (18 × 300 SCF high pressure cylinders), which compressed a 3:1 mixture of H<sub>2</sub>:CO<sub>2</sub> to ~1.4 MPa, where it was then stored in a 240 gal tank. The 240 gal tank fed a second compressor, which compressed the feed to ~5.2 MPa, which was then stored in two 500 gal holding tanks. Next, the high pressure feed was regulated down to the inlet reactor pressure of 2.1 MPa and metered through a control valve with a mass flow meter.

For reverse water–gas shift, the reactor was customized with a 4" diameter sch. 10 stainless steel pipe with an aluminum fin insert to improve heat transfer from the band heaters to the P-K-Mo<sub>2</sub>C/ $\gamma$ -Al<sub>2</sub>O<sub>3</sub> catalyst. The temperature of the reactor was monitored with a thermocouple near the exit of the reactor, while the inlet side of the reactor was charged with aluminum shot to enhance preheating of the reactor feed to 250 °C. Gas exiting the reactor then entered hot and cold traps, the recycle compressor and the back pressure regulator. This reaction produced a stoichiometric amount of water that was captured by a cold trap at 6 °C. The effluent products and residual reactants from the RWGS reactor were sampled by a micro-channel gas chromatograph and logged into LabVIEW. For calculating conversion and selectivity, approximately 8% of the reactor feed was comprised by N<sub>2</sub> as an internal standard.

### DFT calculations of CO<sub>2</sub> and CO adsorption on Mo<sub>2</sub>C

Density functional theory (DFT) calculations were performed within the projector-augmented wave (PAW) method as implemented in the VASP plane-wave DFT software package.<sup>44</sup> The approach was similar to previous work,<sup>45,46</sup> which utilized the Perdew–Burke–Ernzerhof (PBE) formulation<sup>47</sup> of the generalized-gradient approximation (GGA) to the exchange–correlation functional, a 415 eV plane-wave cutoff, gamma-centered  $5 \times 5 \times 1$  *k*-point grid,  $10^{-6}$  eV Å<sup>-1</sup> force convergence criterion, and 1st-order Methfessel–Paxton occupation smearing<sup>48</sup> with 0.2 eV broadening. The supercell consisted of adsorbates plus a slab of  $2 \times 2 \times 1$  unit cells of orthorhombic β-Mo<sub>2</sub>C (48 slab atoms) representing 1.27 nm<sup>2</sup> of the (001) facet. Slabs were constructed with opposing Mo-terminated and C-terminated facets separated by 1.0 nm of vacuum.

Adsorption of CO<sub>2</sub> and CO on the clean, Mo-terminated Mo<sub>2</sub>C(001) facet was considered, as well as in the presence of co-adsorbed oxygen (an oxygen atom bound to each of four

available hollow sites). CO<sub>2</sub> and CO coverages ranged from 0.25 ML (two molecules) to 1 ML (eight molecules). The uppermost Mo and C layers and the adsorbates were allowed to relax, while slab atoms in the lowermost Mo and C layers were fixed in their bulk positions. Supercell dimensions were also fixed during relaxation (1.050 nm × 1.215 nm × 1.455 nm), with in-plane lattice constants of 0.5250 nm and 0.6073 nm obtained from relaxation of the bulk unit cell (in good agreement with experimental values<sup>49</sup> of 0.5195 nm and 0.6022 nm, respectively).

The binding energy per molecule on the surface was calculated using the following equation: BE<sub>ads</sub> = [E[N<sub>ads</sub>@Mo<sub>2</sub>C(001)] – E[Mo<sub>2</sub>C(001)] – N<sub>ads</sub>E<sub>ads</sub>]/N<sub>ads</sub>, where E[N<sub>ads</sub>@Mo<sub>2</sub>C(001)] was the energy of N<sub>ads</sub> CO or CO<sub>2</sub> molecules adsorbed on the clean (or oxidized) Mo<sub>2</sub>C(001) surface, E[Mo<sub>2</sub>C(001)] was the energy of the clean (or oxidized) Mo<sub>2</sub>C surface, and E<sub>ads</sub> was the energy of the CO or CO<sub>2</sub> molecule in the gas phase.

### X-ray photoelectron spectroscopy (XPS)

XPS spectra were gathered over the fresh and spent catalysts using a Kratos Axis Ultra DLD XPS spectrometer equipped with a mono-AlK $\alpha$  X-ray source (1468.6 eV). The XPS spectra were collected using the slot aperture analyzer settings ( $\sim 300 \times 700 \mu\text{m}$  substrate area). Three sweeps were recorded for the survey and regional scans to increase signal-to-noise ratio. The electron collection angle,  $\theta$ , in all XPS measurements was zero. Settings for data collection were: pass energy = 20 eV, dwell time = 200 ms, energy step size = 0.1 eV. Charge compensation was necessary. Calibration of the instrument was confirmed with C 1s peak of carbon tape at 284.6 eV. The XPS signal areas were measured using Casa XPS software.

### N<sub>2</sub> physisorption according to BET method

N<sub>2</sub> physisorption measurements according to BET method were performed using a Micromeritics ASAP 2020 BET Analyzer at  $-196^\circ\text{C}$  to determine catalyst surface area. All of the catalysts were degassed at  $350^\circ\text{C}$  for 2 h under vacuum before analysis.

### Pulse chemisorption

Pulse chemisorption experiments were performed using a Micromeritics AutoChem II 2920, where the probe gas (CO<sub>2</sub> or CO) was pulsed ten times over 50 mg of catalyst at  $35^\circ\text{C}$  to determine the adsorption behavior of the probe molecule. Prior to each measurement, the catalyst was reduced in H<sub>2</sub> for 2 h at  $300^\circ\text{C}$ . Immediately following pulse chemisorption, temperature programmed desorption (TPD) experiments were performed, using the same sample and experimental setup while ramping from  $50^\circ\text{C}$  to  $650^\circ\text{C}$  at a rate of  $5^\circ\text{C min}^{-1}$  under inert He carrier gas flowing at 10 sccm. The blank TPD experiments were performed using the same procedure, but without the pulse chemisorption step.

### X-ray absorption fine structure (XAFS)

X-ray absorption fine structure (XAFS) measurements were used to assess the stability of the P-K-Mo<sub>2</sub>C catalyst *in situ*. XAFS measurements of the Mo K-edge were performed on the 8-ID (ISS)

beamline at the National Synchrotron Light Source (NSLS-II), Brookhaven National Laboratory. Catalysts were diluted with boron nitride, pressed into a pellet, and grinded and sieved between 200–350  $\mu\text{m}$ . The prepared catalyst was then loaded into a custom designed cell with glassy carbon tube with heater and gas connections.<sup>50</sup> The catalysts were reduced *in situ* under hydrogen flow (40 sccm) at  $300^\circ\text{C}$  for 2 h and XAFS data of the Mo K-edge were collected under hydrogen after cooling to room temperature. CO<sub>2</sub> hydrogenation was performed *in situ* under CO<sub>2</sub> and hydrogen flow at 10 sccm and 30 sccm, respectively at  $450^\circ\text{C}$  and  $600^\circ\text{C}$  for 4 h at each temperature. For each temperature, XAFS data of the Mo K-edge were again collected under reaction gases after cooling to room temperature. The incident and transmitted X-ray signals were collected with ionization chambers while the fluorescence signal was collected using a passivated implanted planar silicon (PIPS) detector. The XAFS spectra from the samples were calibrated to a Mo<sub>2</sub>C standard (Alfa Aesar) collected in transmission mode. The X-ray signal was analyzed using the Demeter 0.2.96 data analysis package (Athena, Artemis, Atoms, and FEFF6).<sup>51,52</sup>

## Results

### X-ray diffraction

In addition to the pilot-scale K-Mo<sub>2</sub>C catalyst supported on  $\gamma$ -Al<sub>2</sub>O<sub>3</sub> trilobes (P-K-Mo<sub>2</sub>C/ $\gamma$ -Al<sub>2</sub>O<sub>3</sub>), laboratory-scale K-Mo<sub>2</sub>C supported on  $\gamma$ -Al<sub>2</sub>O<sub>3</sub> powder (L-K-Mo<sub>2</sub>C/ $\gamma$ -Al<sub>2</sub>O<sub>3</sub>) has been synthesized as a reference for comparison with previous work, to assess any discrepancies between the catalysts synthesized on each scale.<sup>41</sup> As a first step to validate synthesis of P-K-Mo<sub>2</sub>C/ $\gamma$ -Al<sub>2</sub>O<sub>3</sub>, the pilot and laboratory-scale catalysts are characterized using X-ray diffraction (XRD).

For P-K-Mo<sub>2</sub>C/ $\gamma$ -Al<sub>2</sub>O<sub>3</sub>, the XRD patterns in Fig. 3 indicate the catalyst is comprised of MoO<sub>2</sub> [PDF: 00-032-0671] and  $\beta$ -Mo<sub>2</sub>C [PDF: 00-035-0787], with large discrete peaks observed at  $26.2^\circ$ ,  $37.0^\circ$ ,  $53.4^\circ$ , and  $60.5^\circ$  for MoO<sub>2</sub> and  $39.3^\circ$  and  $73.4^\circ$  for  $\beta$ -Mo<sub>2</sub>C, suggesting incomplete carburization.<sup>41</sup> Additionally, MoC peaks [PDF: 00-045-1015] are identified at  $2\theta = 35.5^\circ$ ,  $49.0^\circ$  and  $63.8^\circ$ . Reflections due to the trilobe  $\gamma$ -Al<sub>2</sub>O<sub>3</sub> support [PDF: 00-050-0741] are observed at  $2\theta = 37.5^\circ$ ,  $45.5^\circ$  and  $67.0^\circ$ .

For the laboratory as-synthesized catalyst (L-K-Mo<sub>2</sub>C/ $\gamma$ -Al<sub>2</sub>O<sub>3</sub>), no MoO<sub>2</sub> or MoC phases are observed and the reflections corresponding to  $\beta$ -Mo<sub>2</sub>C ( $2\theta = 34.7^\circ$ ,  $39.5^\circ$  and  $61.6^\circ$ ) are observed at relative intensities greatly exceeding that of P-K-Mo<sub>2</sub>C/ $\gamma$ -Al<sub>2</sub>O<sub>3</sub>, suggesting more complete carburization of L-K-Mo<sub>2</sub>C/ $\gamma$ -Al<sub>2</sub>O<sub>3</sub>. This is most likely due to longer carburization of the laboratory-scale catalyst (5 h for L-K-Mo<sub>2</sub>C *versus* 4 h for P-K-Mo<sub>2</sub>C) and improved mass transfer within the  $\gamma$ -Al<sub>2</sub>O<sub>3</sub> powder *versus* the  $\gamma$ -Al<sub>2</sub>O<sub>3</sub> trilobes, even though the P-K-Mo<sub>2</sub>C/ $\gamma$ -Al<sub>2</sub>O<sub>3</sub> is carburized at a higher temperature of  $660^\circ\text{C}$ , *versus*  $600^\circ\text{C}$  for L-K-Mo<sub>2</sub>C/ $\gamma$ -Al<sub>2</sub>O<sub>3</sub>.

### Reactor studies

To first evaluate the performance of the pilot-scale catalyst, P-K-Mo<sub>2</sub>C/ $\gamma$ -Al<sub>2</sub>O<sub>3</sub>, measurements are conducted at the laboratory-scale at several temperatures and under a variety of flow

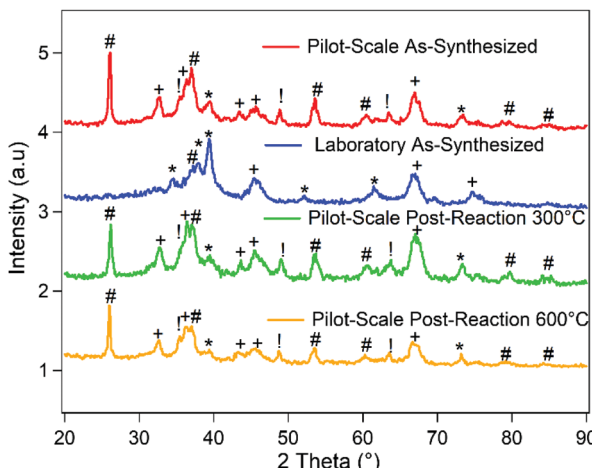


Fig. 3 X-ray diffraction patterns of  $\text{K}-\text{Mo}_2\text{C}/\gamma\text{-Al}_2\text{O}_3$ . Symbols correspond to:  $\gamma\text{-Al}_2\text{O}_3$  (+),  $\text{MoO}_2$  (#),  $\beta\text{-Mo}_2\text{C}$  (\*), and  $\text{MoC}$  (!).

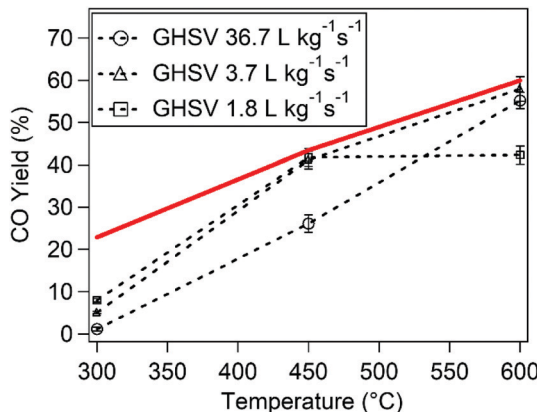


Fig. 4 Performance of  $\text{P-K-Mo}_2\text{C}/\gamma\text{-Al}_2\text{O}_3$  during RWGS at  $300\text{ }^\circ\text{C}$ ,  $450\text{ }^\circ\text{C}$  and  $600\text{ }^\circ\text{C}$  at the laboratory-scale as a function of GHSV. The thermodynamic equilibrium CO yield is plotted as a red solid line. All reactor studies are using a  $3:1\text{ H}_2:\text{CO}_2$  reactant ratio at  $2.1\text{ MPa}$ . All data points are the average of 18 steady-state data points, taken between 7–12 h on stream.

conditions to estimate the ideal experimental regime for pilot-scale studies. As seen in Fig. 4, at  $300\text{ }^\circ\text{C}$ , the CO yield is substantially below the equilibrium value, and decreases slightly as the GHSV is increased. This suggests the reaction is kinetically limited at the highest GHSV of  $36.7\text{ L kg}^{-1}\text{ s}^{-1}$  at  $300\text{ }^\circ\text{C}$ . When the temperature is increased to  $450\text{ }^\circ\text{C}$ , the CO yield approaches equilibrium at  $1.8\text{--}3.7\text{ L kg}^{-1}\text{ s}^{-1}$ , but at the highest GHSV of  $36.7\text{ L kg}^{-1}\text{ s}^{-1}$ , the reaction is kinetically limited. However, at  $600\text{ }^\circ\text{C}$ , the CO yield approaches equilibrium at the higher GHSVs,  $3.7$  and  $36.7\text{ L kg}^{-1}\text{ s}^{-1}$ , likely because of longer space-time at the low GHSV of  $1.8\text{ L kg}^{-1}\text{ s}^{-1}$  resulting in increased  $\text{CO}_2$  methanation. A summary of the laboratory-scale RWGS experiments over  $\text{P-K-Mo}_2\text{C}/\gamma\text{-Al}_2\text{O}_3$  at each temperature and GHSV can be found in Table 1.

To further elaborate on the data contained in Table 1 at  $300\text{ }^\circ\text{C}$  and  $450\text{ }^\circ\text{C}$ , there is a decrease in conversion at increasing GHSV, while CO selectivity remains relatively constant. At  $600\text{ }^\circ\text{C}$ ,

Table 1 Summary of  $\text{P-K-Mo}_2\text{C}/\gamma\text{-Al}_2\text{O}_3$  laboratory-scale reactor performance for RWGS at  $2.1\text{ MPa}$  and  $3:1\text{ H}_2:\text{CO}_2$  ratio as a function of temperature and GHSV. All data points are the average of 18 steady-state data points, taken between 7–12 h on stream. In all cases, no oxygenates are detected

$T$ ( $^\circ\text{C}$ )	GHSV ( $\text{L s}^{-1}\text{ kg}^{-1}$ )	Conversion (%)	Carbon-based selectivity (%)				Carbon balance (%)	CO yield (%)	
			CO	$\text{CH}_4$	$\text{C}_2\text{H}_6$	$\text{C}_2\text{H}_4$			
300	1.1	8.9	99.2	0.6	0.1	0	0	99.4	8.8
300	1.8	8.4	94.9	2.7	1.0	0.1	1.2	99.1	8.0
300	3.7	5.2	98.6	1.1	0.3	0	0	99.2	5.1
300	18.3	2.1	95.7	4.3	0.0	0	0	98.8	2.0
300	36.7	1.2	99.2	0.8	0.0	0	0	99.6	1.2
450	1.1	43.3	95.7	3.5	0.6	0.03	0.15	97.8	41.5
450	1.8	42.1	99.1	0.8	0.1	0	0	100.4	41.7
450	3.7	41.5	99.3	0.5	0.1	0.02	0.14	99.0	41.2
450	18.3	33.0	99.9	0.1	0.0	0.01	0	98.3	33.0
450	36.7	26.2	99.9	0.0	0.0	0.02	0	99.5	26.1
600	1.1	58.5	65.8	31.2	2.7	0	0.3	96.4	38.5
600	1.8	57.6	73.6	23.3	2.7	0	0.5	97.2	42.3
600	3.7	59.0	98.3	1.6	0.1	0	0	98.1	57.9
600	18.3	59.2	98.5	1.4	0.1	0.03	0.03	96.9	58.3
600	36.7	56.3	98.0	1.8	0.1	0.02	0.02	97.9	55.2

there is a slightly different trend, where the conversion is relatively constant, but CO selectivity increases with GHSV because of shorter spacetimes in the reactor, suggesting a  $\text{CO}_2 \rightarrow \text{CO} \rightarrow \text{CH}_4$  mechanism, consistent with work completed by Shi *et al.*<sup>28,53</sup> All data in Table 1 are from steady-state data points averaged between 7–12 h on stream, and it is expected with additional time-on-stream, that the CO selectivities of all  $600\text{ }^\circ\text{C}$  trials would decrease to  $\sim 65\%$ , as shown in the stability measurements in Fig. 5. Additional figures showing the detailed reactor performance of  $\text{P-K-Mo}_2\text{C}/\gamma\text{-Al}_2\text{O}_3$  at each temperature as a function of GHSV can be found in the ESI† (Fig. S7–S9).

From detailed analysis of our laboratory-scale reactor studies in Fig. 4,  $450\text{ }^\circ\text{C}$  is determined to be the optimal temperature for pilot-scale measurements. At the lower temperature of  $300\text{ }^\circ\text{C}$ ,  $\text{P-K-Mo}_2\text{C}$  does not display exceptional performance when compared to other non-precious metal catalysts or the industrial water–gas shift catalyst,  $\text{Cu-ZnO/Al}_2\text{O}_3$ , as shown in Fig. 1 and Table 4. At  $600\text{ }^\circ\text{C}$ , the  $\text{P-K-Mo}_2\text{C}$  catalyst transitions from a highly selective RWGS catalyst to a methanation catalyst after only  $\sim 14$  h on stream, as shown in Fig. 5. Therefore,  $450\text{ }^\circ\text{C}$  is the most appropriate temperature for pilot-scale studies, because at this temperature,  $\text{P-K-Mo}_2\text{C}$  demonstrates high  $\text{CO}_2$  conversion, CO selectivity and stability.

As shown in Fig. 6 for the scaled-up reactor studies of  $\text{P-K-Mo}_2\text{C}/\gamma\text{-Al}_2\text{O}_3$ , the catalyst displays consistently high  $\text{CO}_2$  conversion and CO selectivity at  $450\text{ }^\circ\text{C}$  across a range of GHSVs. The piping and instrumentation diagram for the pilot-scale reactor is included in Fig. S6 of the ESI.†

The CO yield for the data point at the GHSV of  $\sim 0.5\text{ L kg}^{-1}\text{ s}^{-1}$  in Fig. 6 appears to exceed the maximum thermodynamic equilibrium, but this value is within the margin of error and is likely an artifact of slight variations in the inlet reactant mixture at flow rates greater than 60 standard liters per minute (SLPM) during the pilot-scale studies. Similar to the laboratory-scale experiments, the performance of  $\text{P-K-Mo}_2\text{C}/\gamma\text{-Al}_2\text{O}_3$  at  $450\text{ }^\circ\text{C}$  does not appear to be

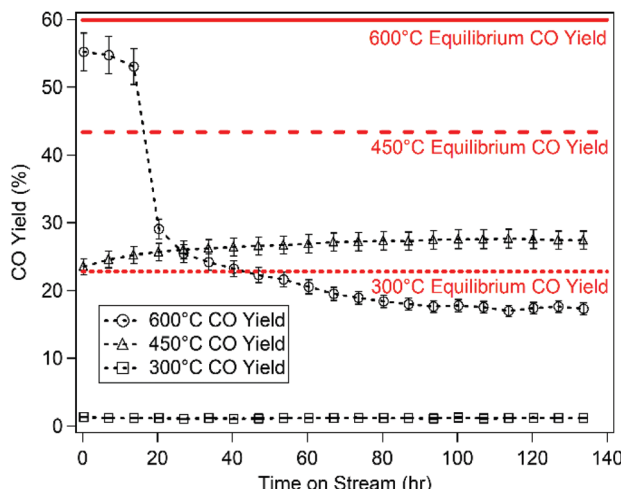


Fig. 5 Laboratory-scale performance of P-K-Mo<sub>2</sub>C/γ-Al<sub>2</sub>O<sub>3</sub> during RWGS for 120 h on stream. CO yield versus time-on-stream is plotted for experimental data (markers) and the equilibrium maximum CO yields (red lines) at each temperature. Experiments are all at a GHSV of 36.7 L kg<sup>-1</sup> s<sup>-1</sup> with a 3:1 H<sub>2</sub>:CO<sub>2</sub> reactant ratio at the temperatures listed (300 °C, 450 °C, 600 °C) and 2.1 MPa.

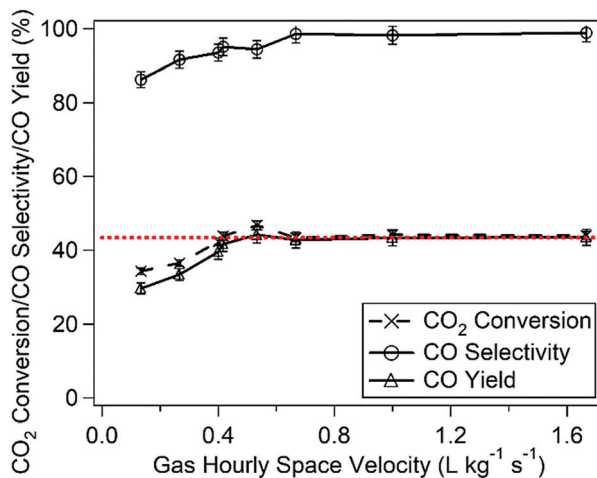


Fig. 6 Pilot-scale reactor performance of P-K-Mo<sub>2</sub>C/γ-Al<sub>2</sub>O<sub>3</sub> during RWGS with CO<sub>2</sub> conversion, CO selectivity and CO yield plotted versus GHSV. The thermodynamically limited equilibrium CO yield of RWGS is included as a dotted red line. All reactor studies are for a 3:1 H<sub>2</sub>:CO<sub>2</sub> reactant ratio at 450 °C and 2.1 MPa.

a strong function of GHSV, which is likely due to thermodynamic limitations of the reaction under the tested conditions. Higher flow conditions could not be tested at the pilot-scale because the experimental apparatus (details in the Experimental section) prevented the H<sub>2</sub> flow rate from exceeding ~150 SLPM.

The observed equilibrium limitations of the pilot-scale reactor experiments at 450 °C, shown in Fig. 6, require additional experiments at higher GHSVs to both determine the catalytic performance in the kinetically limited regime and accurately assess the stability for future scale-up. As shown in the stability measurements in Fig. 5, laboratory-scale, time-on-stream reactor studies of P-K-Mo<sub>2</sub>C/γ-Al<sub>2</sub>O<sub>3</sub> at 450 °C and a GHSV of 36.7 L kg<sup>-1</sup> s<sup>-1</sup>, exhibit

no signs of deactivation for 120 h on stream, with a CO yield and STY equal to 26.6% and 99.1 μmol CO g<sup>-1</sup> s<sup>-1</sup>, respectively. This suggests that during scale-up, GHSVs can be used that are ~20× faster than those in the pilot-scale study to maximize the CO STY at 450 °C.

For time-on-stream experiments at 300 °C, the CO yield is also stable at 1.2%, but there is a significant decrease (~71%) observed in the CO yield of the catalyst tested at 600 °C after ~14 h on stream. The conversion over the catalyst tested at 600 °C remains relatively constant, but the decrease in CO yield is due to a substantial decrease in CO selectivity with a corresponding increase in CH<sub>4</sub> selectivity. After regenerating the catalyst with H<sub>2</sub> for 2 h at 300 °C, the CO selectivity recovers slightly from 28.8% to 41.0%, but does not reach the original value of 98.1%.

Although the single-pass CO yield is thermodynamically limited to 43.4% at 450 °C with a 3:1 H<sub>2</sub>:CO<sub>2</sub> ratio, the maximum CO yield can be increased by recycling the single-pass product stream, as shown in Fig. 7. With each recycle trial, the fresh feed flow rate is kept constant at 60 SLPM and a fraction of the reactor effluent is chilled to 6 °C to remove water, preheated, and then mixed with the fresh feed to yield GHSVs over the catalyst from 1.7 L kg<sup>-1</sup> s<sup>-1</sup> to 5.1 L kg<sup>-1</sup> s<sup>-1</sup>. The recycle ratio plotted in Fig. 7 is the ratio between the molar flow rate of the recycled reactor effluent and the fresh feed entering the reactor. As shown in the figure, the CO<sub>2</sub> conversion increases steadily as a function of recycle ratio, as expected.

It is also observed that the CO selectivity decreases with increasing recycle ratio, suggesting that the longer average residence times of CO<sub>2</sub> and CO within the reactor result in higher conversion, but lower CO selectivity. At the highest recycle ratio of 2, the reactor effluent is ~18% CO and only 5.6% CO<sub>2</sub>, indicating the outlet CO:CO<sub>2</sub> ratio is ~3, while during

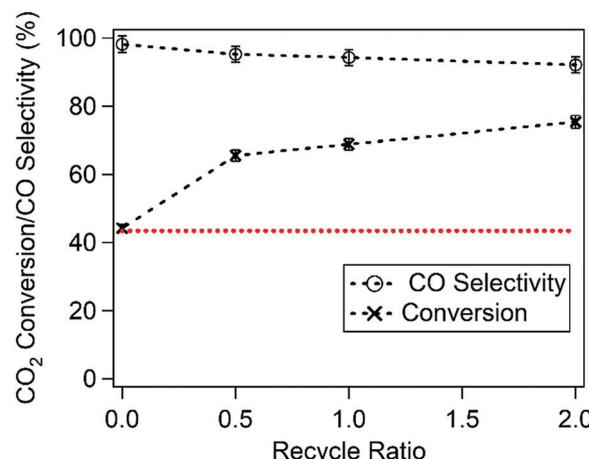


Fig. 7 Pilot-scale reactor performance of P-K-Mo<sub>2</sub>C/γ-Al<sub>2</sub>O<sub>3</sub> during RWGS with recycle. CO<sub>2</sub> conversion and CO selectivity are plotted versus recycle ratio for 1 kg of catalyst with a constant fresh feed flow rate of 60 SLPM and GHSVs over the catalyst from 1.7 L kg<sup>-1</sup> s<sup>-1</sup> to 5.1 L kg<sup>-1</sup> s<sup>-1</sup>. Single pass equilibrium conversion for these reaction conditions is plotted as a dotted red line. All reactor studies are for a 3:1 H<sub>2</sub>:CO<sub>2</sub> reactant ratio at 450 °C and 2.1 MPa.

single pass conversion the outlet CO:CO<sub>2</sub> ratio is ~0.8. Therefore, the higher concentration of CO combined with greater residence time during recycle, results in a larger fraction of CO hydrogenated to undesired CH<sub>4</sub>. However, CO selectivity remains above 92% in all cases, demonstrating recycling is an effective tool to increase the CO yield at lower temperatures. It is also important to note that all pilot-scale studies were conducted sequentially without any re-activation steps. Total time-on-stream was approximately 10 days and the catalyst exhibited no signs of deactivation.

### Density functional theory calculations

In an effort to better explain the decreasing CO selectivity at high recycle ratios, DFT calculations are shown in Fig. 8 and 9 to quantify the strength of CO<sub>2</sub> and CO adsorption over clean Mo<sub>2</sub>C and Mo<sub>2</sub>C modified with oxygen, which models the active oxycarbide phase of the RWGS reaction.<sup>30</sup> As shown in Fig. 8, CO<sub>2</sub> and CO both adsorb favorably to Mo<sub>2</sub>C and oxygen-modified Mo<sub>2</sub>C.<sup>54</sup> Closer inspection of the figure reveals that at all CO<sub>2</sub> and CO coverages between 0.25 and 1 ML, CO adsorbs more strongly than CO<sub>2</sub> to the Mo<sub>2</sub>C-based surface. This is an important result that corroborates the findings of the pilot-scale recycle study where a decrease in CO selectivity is observed at high recycle ratios. A likely cause of the decreasing CO selectivity is that during single pass conversion, CO<sub>2</sub> is the primary carbon-based species in the reactor and has active sites available for reaction, resulting in a CO selectivity of 98.2%. As the recycle ratio increases to 2, the CO:CO<sub>2</sub> ratio within the reactor also increases from 0.8 to 3, resulting in high CO coverage on the catalyst surface.

These results agree with the DFT calculations of adsorbates over oxygen-modified Mo<sub>2</sub>C in Fig. 8, where CO binds much

more strongly (~38 kcal mol<sup>-1</sup> at 1 ML) than CO<sub>2</sub> (~7 kcal mol<sup>-1</sup> at 1 ML), resulting in hydrogenation of CO to CH<sub>4</sub>, with the gradual decrease in CO selectivity from 98.2% to 92.1%. An example of the adsorption configurations for both the clean and O-covered Mo<sub>2</sub>C is included as Fig. S10 of the ESI.†

### X-ray photoelectron spectroscopy

To gain additional insight into the active phase of K-Mo<sub>2</sub>C/γ-Al<sub>2</sub>O<sub>3</sub> that results in high performance for RWGS, X-ray photoelectron spectroscopy (XPS) measurements of the Mo 3d, C 1s and O 1s electrons are conducted for the lab-scale and pilot-scale K-Mo<sub>2</sub>C/γ-Al<sub>2</sub>O<sub>3</sub>. The high stability of P-K-Mo<sub>2</sub>C/γ-Al<sub>2</sub>O<sub>3</sub> at 300 °C and 450 °C, but transient behavior at 600 °C, suggests that the active phase of the catalyst could be dynamic under the high temperature conditions.

The quantitative *ex situ* Mo 3d composition of each catalyst from XPS deconvolution can be found in Fig. 10 and Table 2, with values of binding energy for each Mo species taken from Oshikawa *et al.*<sup>56</sup> From examining the Mo oxidation state composition before and after the pilot-scale reaction at each temperature, it is clear that during reaction, the metallic Mo phase of the catalyst surface becomes oxidized to contribute to an increase in MoO<sub>3</sub> (Mo<sup>6+</sup>). Additionally, within the pilot-scale P-K-Mo<sub>2</sub>C/γ-Al<sub>2</sub>O<sub>3</sub> catalyst, the Mo<sup>4+</sup> composition, which represents MoO<sub>2</sub>, is relatively unchanged after the reaction at 300 °C and 450 °C. These findings generally support the observations of the XRD patterns shown in Fig. 3, where significant changes to the bulk crystalline structure of the catalyst do not occur during reaction.

The exception is at 600 °C, where XRD in Fig. 3 indicates no significant deformations to bulk crystalline structure, yet the

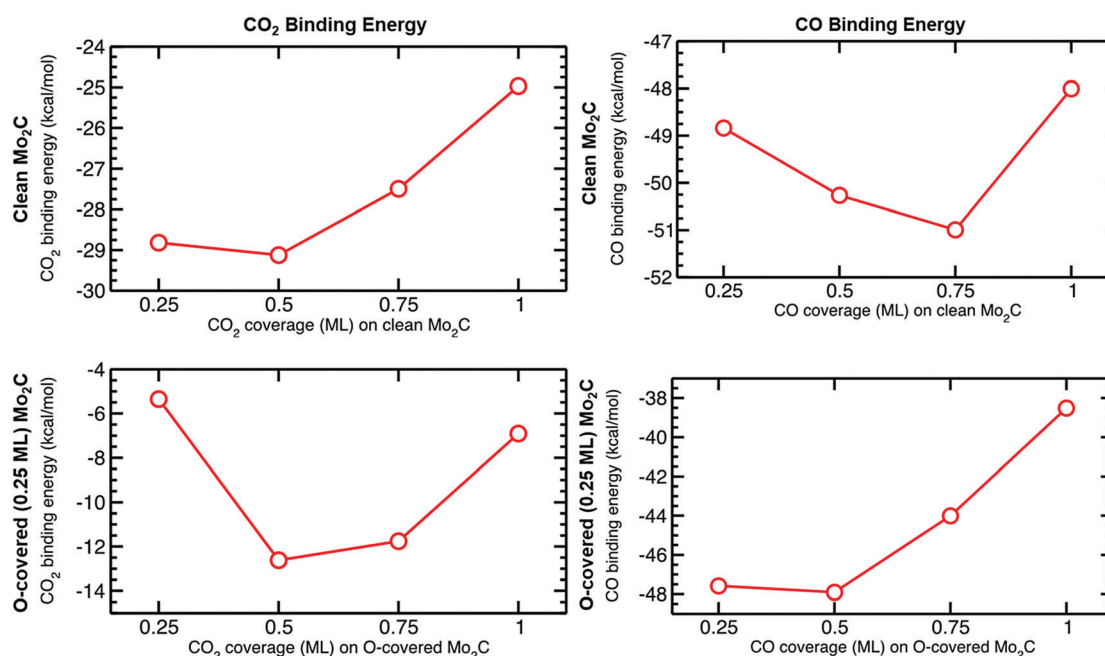
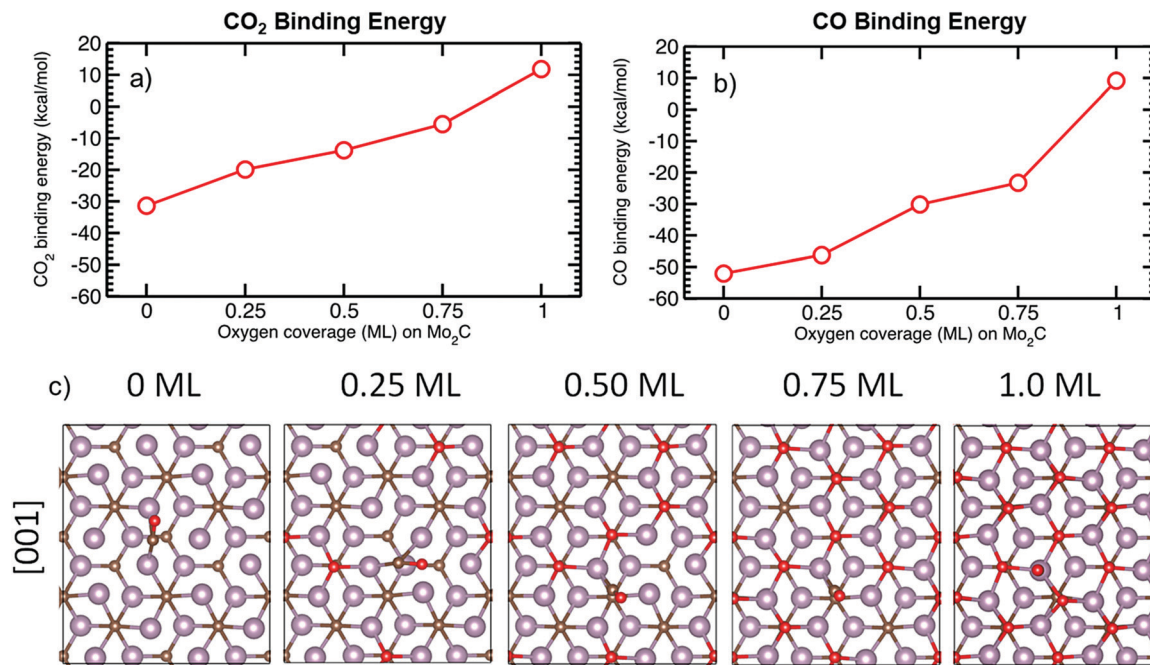
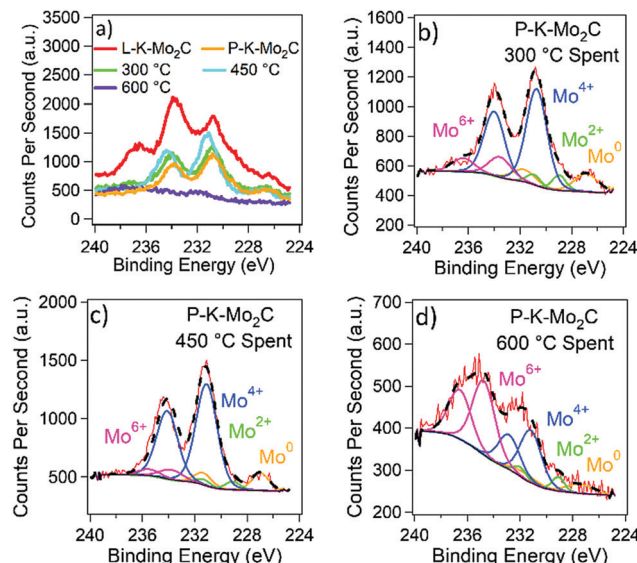


Fig. 8 DFT calculations displaying CO<sub>2</sub> and CO adsorption energies for clean Mo<sub>2</sub>C and O-covered (0.25 ML) Mo<sub>2</sub>C as a function of CO<sub>2</sub> and CO coverage.



**Fig. 9** Binding energies of single (a) CO<sub>2</sub>; and (b) CO molecules as a function of oxygen coverage on the Mo-terminated Mo<sub>2</sub>C surface; (c) adsorption configurations of CO on the Mo-terminated Mo<sub>2</sub>C surface with oxygen coverage ranging from 0 ML to 1.0 ML, viewed along the [001] crystal axis. Binding is endothermic for oxygen coverage larger than 0.75 ML for both CO and CO<sub>2</sub> molecules. CO<sub>2</sub> adsorption data is reproduced from ref. 55.



**Fig. 10** (a) Mo 3d spectra of as-synthesized L-K-Mo<sub>2</sub>C/γ-Al<sub>2</sub>O<sub>3</sub> and P-K-Mo<sub>2</sub>C/γ-Al<sub>2</sub>O<sub>3</sub> (dashed black lines), with spectra included of P-K-Mo<sub>2</sub>C/γ-Al<sub>2</sub>O<sub>3</sub> after laboratory-scale reaction at 300 °C, 450 °C and 600 °C. Deconvoluted Mo 3d spectra (solid line) of P-K-Mo<sub>2</sub>C/γ-Al<sub>2</sub>O<sub>3</sub> with fits (dashed line) after 12 h on stream at (b) 300 °C; (c) 450 °C; and (d) 600 °C. Contributions include Mo<sup>6+</sup>, Mo<sup>4+</sup>, Mo<sup>2+</sup> and Mo<sup>0</sup>.

XPS spectra of the Mo 3d electron exhibits significant increases to the Mo<sup>6+</sup> contribution, with a corresponding decrease to Mo<sup>4+</sup>. Careful inspection of the data in Fig. 10 shows much lower counts per second for the spent catalyst at 600 °C *versus* the other samples, suggesting coking of the active Mo phase at

**Table 2** Composition of deconvoluted XPS spectra for K-Mo<sub>2</sub>C/γ-Al<sub>2</sub>O<sub>3</sub> before and after laboratory-scale RWGS reaction at 300 °C, 450 °C and 600 °C at a GHSV of 1.7 L kg<sup>-1</sup> s<sup>-1</sup> for a 3:1 H<sub>2</sub>:CO<sub>2</sub> ratio at 2.1 MPa

Catalyst	Mo <sup>0</sup>	Mo <sup>2+</sup>	Mo <sup>4+</sup>	Mo <sup>6+</sup>
L-K-Mo <sub>2</sub> C as-synthesized	6.6	14.8	39.5	39.0
P-K-Mo <sub>2</sub> C as-synthesized	13.8	14.9	56.9	14.5
P-K-Mo <sub>2</sub> C 300 °C post-reaction	13.9	6.8	64.8	14.5
P-K-Mo <sub>2</sub> C 450 °C post-reaction	10.9	4.4	77.0	7.7
P-K-Mo <sub>2</sub> C 600 °C post-reaction	2.0	7.0	46.9	44.1

600 °C, which is further supported by the high C 1s counts in Fig. 11. Additionally, as shown in the deconvoluted XPS quantification in Table 2, the decrease in Mo<sup>4+</sup> composition at 600 °C is accompanied by a corresponding increase to Mo<sup>6+</sup>, indicating that MoO<sub>2</sub> is further oxidized during reaction, likely causing the decrease in CO selectivity at 600 °C observed in Fig. 5, due to the electronic modification of Mo sites by oxygen that results in the dramatically different adsorption behavior of CO *versus* CO<sub>2</sub> as described in the DFT calculations in Fig. 8 and 9.<sup>55</sup>

This XPS characterization supports previous conclusions emphasizing the dynamic oxidation state of Mo<sub>2</sub>C-based catalysts under reaction conditions.<sup>41</sup> Additional deconvolution of XPS spectra for the as-synthesized P-K-Mo<sub>2</sub>C/γ-Al<sub>2</sub>O<sub>3</sub> and L-K-Mo<sub>2</sub>C/γ-Al<sub>2</sub>O<sub>3</sub> are found in Fig. S11, S12 and Table S3 of the ESI.<sup>†</sup>

To further investigate trends between catalytic structure and performance, analysis of the C 1s XPS spectra of the as-synthesized and spent catalysts is shown in Fig. 11. Formation of the active carbide phase can be assigned to a C–Mo peak

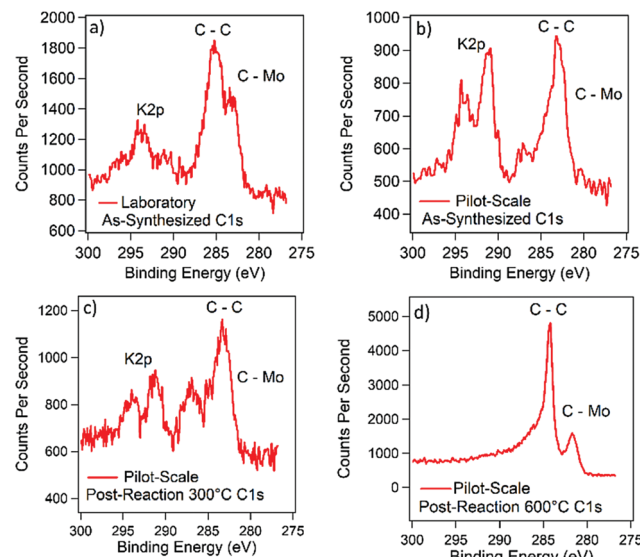


**Fig. 11** C 1s XPS spectra for (a) as-synthesized L-K-Mo<sub>2</sub>C/γ-Al<sub>2</sub>O<sub>3</sub>; (b) as-synthesized P-K-Mo<sub>2</sub>C; (c) P-K-Mo<sub>2</sub>C/γ-Al<sub>2</sub>O<sub>3</sub> after reaction at 300 °C; and (d) P-K-Mo<sub>2</sub>C/γ-Al<sub>2</sub>O<sub>3</sub> after reaction at 600 °C. XPS spectra are recorded ex-situ after 12 h on stream in the laboratory with 3:1 H<sub>2</sub>:CO<sub>2</sub> ratio at 2.1 MPa.

at 283.3 eV.<sup>56</sup> For the pilot-scale catalyst before and after reaction at 300 °C, a C-Mo shoulder cannot be clearly identified in Fig. 11. The C-Mo shoulder could be enveloped by the graphitic carbon peak, or the XPS spectra is providing further evidence that carburization of P-K-Mo<sub>2</sub>C/γ-Al<sub>2</sub>O<sub>3</sub> is incomplete, which is supported by the XRD spectra in Fig. 3. The peaks at higher binding energies can be attributed to the K 2p signal of potassium, present within the K-Mo<sub>2</sub>C catalyst.<sup>57</sup> As observed in the spectra, this signal between 290–295 eV remains relatively constant as compared to the graphitic carbon peak, both before and after reaction at 300 °C, suggesting minimal coking of the catalyst surface under these reaction conditions.<sup>58</sup> However, for P-K-Mo<sub>2</sub>C/γ-Al<sub>2</sub>O<sub>3</sub> reacted at 600 °C, the C-C peak dominates the spectra, indicating that the surface of the catalyst becomes covered in coke at the high temperature reaction conditions, potentially leading to the transient catalyst behavior, and in turn, the CH<sub>4</sub> formation observed during reactor studies.<sup>58</sup>

Analysis of the O 1s XPS spectra of the as-synthesized and spent catalysts (Fig. S13 of the ESI†) shows formation of a distinct O-Mo peak at 531 eV for all catalysts. The O-Mo peak could be characteristic of an oxycarbide, the active phase for RWGS.<sup>54</sup> The P-K-Mo<sub>2</sub>C/γ-Al<sub>2</sub>O<sub>3</sub> catalyst after laboratory-scale

reaction 600 °C displays an additional oxide peak associated with carbonate species at ~536 eV, which provides evidence that oxidation is attributing to the increase in CH<sub>4</sub> selectivity, as carbonate species are common intermediates during CO<sub>2</sub> methanation.<sup>58,59</sup> At temperatures of 600 °C, carburization begins over Mo-based catalysts, which suggests a dynamic surface structure and limited catalyst stability under these high temperature conditions, despite unchanged bulk structure as evidenced by the XRD patterns in Fig. 3.<sup>58</sup>

### Pulse chemisorption and temperature programmed desorption

To gain a better understanding of the relationship between reactor performance and catalyst structure, N<sub>2</sub> physisorption according to BET method of the P-K-Mo<sub>2</sub>C/γ-Al<sub>2</sub>O<sub>3</sub> catalyst before and after reaction is shown in Table 3. As shown in the table, there is a decrease in N<sub>2</sub> physisorption according to BET method after reaction. Although there is little change observed in the textural properties of the catalyst during RWGS, pulse chemisorption of the CO<sub>2</sub> reactant and CO product can provide further insight into the dynamic changes in catalyst structure observed in the XPS data.

As shown in Table 3, we also observe a much larger amount of CO<sub>2</sub> adsorbed relative to CO for the as-synthesized P-K-Mo<sub>2</sub>C/γ-Al<sub>2</sub>O<sub>3</sub>, which is favorable for high CO selectivity during RWGS. This is likely from the large surface concentration of potassium seen in the C 1s XPS in Fig. 11b, which provides basic sites that are favorable for CO<sub>2</sub> adsorption prior to reaction. However, for all catalysts after reaction, there is an order of magnitude decrease of chemisorbed CO<sub>2</sub>, combined with a corresponding increase in adsorbed CO. The decrease of chemisorbed CO<sub>2</sub> on K-Mo<sub>2</sub>C could be due to surface oxidation that occurs during CO<sub>2</sub> dissociation,<sup>28,53</sup> decrease in surface K, as shown by XPS in Fig. 11, and/or coking that occurs during reaction. If the surface of the catalyst becomes oxidized, this likely leads to a more pronounced decrease in CO<sub>2</sub> coverage relative to CO, supported by the aforementioned DFT calculations in Fig. 8 and 9. Additionally, coke formation would significantly decrease the affinity of the catalyst to CO<sub>2</sub>, as suggested by DFT calculations in Fig. S14 (ESI†), revealing weak binding of CO<sub>2</sub> (−1.06 kcal mol<sup>−1</sup>) on C-terminated Mo<sub>2</sub>C. This behavior is consistent with the decrease in CO<sub>2</sub> coverage after reaction.

To further probe the adsorption behavior of CO<sub>2</sub>, temperature programmed desorption (TPD) experiments are shown in Fig. 12. When examining the relative binding strength of CO<sub>2</sub> over the as-synthesized and P-K-Mo<sub>2</sub>C/γ-Al<sub>2</sub>O<sub>3</sub> reacted at 300 °C, 450 °C and 600 °C, the overall shape of the TPD profiles are

**Table 3** N<sub>2</sub> physisorption and total pore volume according to BET method and CO<sub>2</sub> and CO chemisorption over Mo<sub>2</sub>C/γ-Al<sub>2</sub>O<sub>3</sub> as-synthesized and after laboratory-scale reaction at 300 °C, 450 °C and 600 °C

P-K-Mo <sub>2</sub> C condition	N <sub>2</sub> physisorption (m <sup>2</sup> g <sup>−1</sup> )	Total pore volume (cm <sup>3</sup> g <sup>−1</sup> )	CO <sub>2</sub> quantity adsorbed (μmol g <sup>−1</sup> )	CO quantity adsorbed (μmol g <sup>−1</sup> )
As-synthesized	142	0.6	29.5	0.2
300 °C post-reaction	138	0.6	4.3	1.2
450 °C post-reaction	115	0.5	1.1	1.0
600 °C post-reaction	120	0.6	2.7	1.7

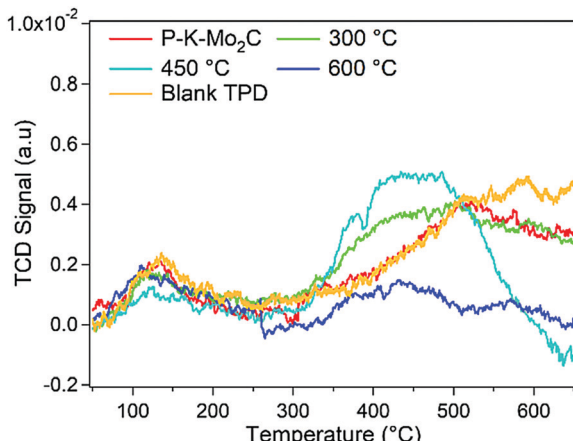


**Fig. 12**  $\text{CO}_2$ -TPD for as-synthesized (red) and spent P-K-Mo<sub>2</sub>C/ $\gamma$ -Al<sub>2</sub>O<sub>3</sub> after 12 h on stream at 300 °C (green), 450 °C (teal) and 600 °C (blue) from 50 °C to 650 °C with a ramp rate of 5 °C min<sup>-1</sup>.

fairly similar with a few exceptions. Each profile generally contains a broad desorption peak at ~400 °C, while the peak for the as-synthesized catalyst is shifted toward a higher temperature. For the CO-TPD in Fig. S15 (ESI†), similar desorption behavior is observed as the  $\text{CO}_2$ -TPD profile in Fig. 12, suggesting that  $\text{CO}_2$  and CO adsorb on the same active sites over K-Mo<sub>2</sub>C/ $\gamma$ -Al<sub>2</sub>O<sub>3</sub>.

A significant exception is the  $\text{CO}_2$ -TPD profile for P-K-Mo<sub>2</sub>C/ $\gamma$ -Al<sub>2</sub>O<sub>3</sub> after reaction at 450 °C, which is both broader and larger than the TPD profiles of the other conditions. These data suggest that the high performance observed in the reactor at 450 °C could be a result of either: (1) improved dissociation of adsorbed  $\text{CO}_2$  into CO; or (2) rapid  $\text{CO}_2$  and CO adsorption/desorption, potentially minimizing any desorption limitations on the reaction kinetics.

For the 600 °C trial, the decrease in CO selectivity and corresponding increase in CH<sub>4</sub> selectivity (Fig. 5) is correlated with a relative decrease in intensity of the peak at 450 °C. This could suggest that CO<sub>2</sub> and CO exhibit stronger adsorption over the P-K-Mo<sub>2</sub>C/ $\gamma$ -Al<sub>2</sub>O<sub>3</sub> reacted at 600 °C, which results in a net increase in the rate of CO hydrogenation to CH<sub>4</sub>, and in turn, higher CH<sub>4</sub> selectivity. It is important to note, however, that the TPD experiments are measuring the composition of the effluent gas with a thermal conductivity detector (TCD), so we performed additional experiments to test for decomposition of the catalyst. These experiments are particularly important, because large peaks are observed during the TPD experiments at high temperature ~700 °C in Fig. S16 (ESI†).

To understand if there is any significant catalyst decomposition that would affect the reaction, Fig. S17a (ESI†) shows the Mo K-edge X-ray absorption near-edge structure (XANES) spectra of the P-K-Mo<sub>2</sub>C catalyst as-synthesized and after reduction. Careful examination of the Mo K-edge XANES in Fig. S17a (ESI†) shows a slight shift of the first peak located at approximately 20010 eV toward lower energies, which is associated with partial reduction of the MoO<sub>3</sub> passivation layer after reduction. More importantly, when comparing the reduced catalyst with the catalyst after reaction at 450 °C and 600 °C

in Fig. S17b (ESI†), it is clear that all catalysts are relatively stable during the reaction. When combined with the reactor data and CO<sub>2</sub> and CO TPDS in Fig. 12 and Fig. S15 (ESI†), respectively, these XANES data provide further support that the catalyst is stable and not decomposing during reaction.

## Discussion

As shown in the Results section, P-K-Mo<sub>2</sub>C/ $\gamma$ -Al<sub>2</sub>O<sub>3</sub> exhibits high performance for the RWGS reaction at both the laboratory and pilot-scales, with minimal deactivation and >95% CO selectivity under most reaction conditions. In assessing the viability for scale-up, there is a reported difference between the range of GHSVs tested at each scale. Clearly, P-K-Mo<sub>2</sub>C/ $\gamma$ -Al<sub>2</sub>O<sub>3</sub> under pilot-scale conditions is equilibrium and/or mass-transfer limited because reactant flow rates above 200 SLPM could not be achieved, but higher GHSVs (36.7 L kg<sup>-1</sup> s<sup>-1</sup>) have been measured in the laboratory to test catalytic stability in the kinetically limited regime. Nevertheless, there is good agreement between the laboratory and pilot-scale reactor data, providing strong evidence that the P-K-Mo<sub>2</sub>C/ $\gamma$ -Al<sub>2</sub>O<sub>3</sub> catalyst has high potential for scale-up as part of an industrial  $\text{CO}_2$  hydrogenation process. It is important to note, however, that there are distinct differences between the K-Mo<sub>2</sub>C/ $\gamma$ -Al<sub>2</sub>O<sub>3</sub> catalyst synthesized on the laboratory and pilot-scales. This is illustrated in the reactor data in Table 4, where P-K-Mo<sub>2</sub>C/ $\gamma$ -Al<sub>2</sub>O<sub>3</sub> exhibits improved performance, illustrated by the ~25% higher CO STY, relative to what has been previously reported for L-K-Mo<sub>2</sub>C/ $\gamma$ -Al<sub>2</sub>O<sub>3</sub> under analogous reaction conditions,<sup>41</sup> requiring further characterization to understand the cause of this discrepancy.

The difference in catalytic performance can be explained by the differences in bulk crystalline structure observed between the pilot and laboratory-scale catalysts, which is a result of slight differences in catalyst synthesis, outlined in the Experimental section. In brief, for P-K-Mo<sub>2</sub>C/ $\gamma$ -Al<sub>2</sub>O<sub>3</sub>, the molybdenum and potassium precursors are introduced into the  $\gamma$ -Al<sub>2</sub>O<sub>3</sub> trilobe support from St. Gobain via three-step incipient wetness impregnation with a molar ratio of 1/4/15 K/Mo/ $\gamma$ -Al<sub>2</sub>O<sub>3</sub>. After impregnation, the catalyst is calcined, carburized for 4 h at 660 °C and passivated.

The laboratory-scale synthesis procedure is similar, but the  $\gamma$ -Al<sub>2</sub>O<sub>3</sub> is a powder sourced from Alfa Aesar and the catalyst is carburized for 5 h at 600 °C. Another key distinction between these synthesis procedures is the batch size of the final Mo<sub>2</sub>C-based catalyst. The pilot-scale procedure results in a yield of ~3 kg of catalyst, while the laboratory-scale synthesis yields ~3 g. Although the overall procedures are mostly analogous, it is likely that heat and/or mass transfer differences during pilot-scale carburization result in the incomplete carburization of P-K-Mo<sub>2</sub>C, observed in the XRD in Fig. 3 and XPS in Fig. 10 and 11.

To address the discrepancy in carburization conditions, we performed additional experiments where we calcined the P-K-Mo<sub>2</sub>C (350 °C for 6 h), then recarburized the catalyst under

**Table 4** Comparison of P-K-Mo<sub>2</sub>C/γ-Al<sub>2</sub>O<sub>3</sub> with other high-performance RWGS catalysts at varying conditions for benchmarking catalytic performance. The asterisk (\*) indicates this work. The P-K-Mo<sub>2</sub>C/γ-Al<sub>2</sub>O<sub>3</sub> trial marked with (ϕ) has been conducted with the pilot-scale reactor. All other reaction trials marked with an asterisk (\*) have been performed using the laboratory-scale reactor. (‡) The Argus metals database was utilized to obtain active metal costs on a per gram basis for the CO cost (\$ metal kg CO<sup>-1</sup>) calculation. Further details regarding the reaction conditions are included within the Experimental section. For catalysts with greater than 2% of carbon as C<sub>3+</sub> products, a detailed distribution of products is provided in the ESI in Table S4 and additional catalysts for benchmarking are included in Table S5 (ESI). In all cases, no oxygenates are detected

Catalyst	T (°C)	P (MPa)	H <sub>2</sub> :CO <sub>2</sub> ratio	GHSV (L kg <sup>-1</sup> s <sup>-1</sup> )	Conversion (%)	Carbon-based selectivity (%)			CO yield (%)	CO STY (μmol CO gcat <sup>-1</sup> s <sup>-1</sup> )	CO production rate (kg CO day <sup>-1</sup> )	CO cost (\$ metal kg CO <sup>-1</sup> ) <sup>‡</sup>
						CO	CH <sub>4</sub>	C <sub>2</sub> H <sub>6</sub> and C <sub>2</sub> H <sub>4</sub>				
*L-K-Mo <sub>2</sub> C/γ-Al <sub>2</sub> O <sub>3</sub>	450	2.1	3	36.7	22.1	97.3	2.0	0.7	0.0	21.5	80.0	984.2
*P-K-Mo <sub>2</sub> C/γ-Al <sub>2</sub> O <sub>3</sub>	450	2.1	3	36.7	26.8	99.3	0.3	0.4	0.0	26.6	99.1	1219.0
*LC-P-Mo <sub>2</sub> C/γ-Al <sub>2</sub> O <sub>3</sub>	450	2.1	3	36.7	42.7	99.1	0.6	0.3	0.0	42.4	157.7	1940.1
*P-K-Mo <sub>2</sub> C/γ-Al <sub>2</sub> O <sub>3</sub>	450	2.1	3	18.3	33.1	99.88	0.09	0.03	0.0	33.0	61.4	755.6
*P-K-Mo <sub>2</sub> C/γ-Al <sub>2</sub> O <sub>3</sub>	450	2.1	3	1.8	42.1	99.1	0.8	0.2	0.2	41.7	7.8	95.5
ϕP-K-Mo <sub>2</sub> C/γ-Al <sub>2</sub> O <sub>3</sub>	450	2.1	3	1.7	48	98.9	1.1	0.0	0.0	47.5	8.8	97.8
*P-K-Mo <sub>2</sub> C/γ-Al <sub>2</sub> O <sub>3</sub>	450	0.1	3	1.8	21.1	93.3	6.0	0.7	0.0	19.7	3.7	45.1
*P-K-Mo <sub>2</sub> C/γ-Al <sub>2</sub> O <sub>3</sub>	600	2.1	3	3.7	59.0	98.1	1.8	0.1	0.0	57.9	21.5	265.0
*Revitalized	600	2.1	3	3.7	58.7	43.2	52.1	4.0	0.7	25.4	9.4	116.2
P-K-Mo <sub>2</sub> C/γ-Al <sub>2</sub> O <sub>3</sub>												
*P-K-Mo <sub>2</sub> C/γ-Al <sub>2</sub> O <sub>3</sub>	300	2.1	3	36.7	1.2	99.2	0.8	0.0	0.0	1.2	4.3	52.9
*Cu-ZnO/Al <sub>2</sub> O <sub>3</sub>	300	2.1	3	36.7	23.3	92.6	4.6	2.8	0.0	21.6	80.2	194.0
*FeCrO <sub>x</sub>	450	2.1	3	36.7	47.5	48.6	37.3	7.3	6.8	23.1	85.8	207.7
Rh/S-1 <sup>22</sup>	450	1	3	3.3	38.0	71.3	28.7	N/A	N/A	27.1	3.0	1828.8
InNi <sub>3</sub> C <sub>0.5</sub> /Al <sub>2</sub> O <sub>3</sub> <sup>92</sup>	420	1	3	6.0	35.6	88.8	1.0	10.2	N/A	31.6	10.35	30.9
Pt/TiO <sub>2</sub> <sup>23</sup>	400	0.1	1	1.7	14.9	100.0	0.0	N/A	N/A	14.9	5.0	1231.5
Fe/CeO <sub>2</sub> <sup>25</sup>	400	0.1	4	16.7	8.1	100.0	0.0	N/A	N/A	8.7	6.5	208.6
Cu/CeO <sub>2</sub> <sup>25</sup>	400	0.1	4	16.7	31.3	100.0	0.0	N/A	N/A	31.3	23.3	667.6
Fe/TiO <sub>2</sub> <sup>93</sup>	270	2.0	3	2.2	2.7	73.0	11.6	5.1	10.3	1.9	0.96	92.9

laboratory-scale conditions (LC-P-Mo<sub>2</sub>C) to understand if the scaled-up carburization affects RWGS performance. The XRD and XPS of the recarburized catalyst can be found in the ESI† (Fig. S18 and S19). We also include reactor studies over the recarburized catalyst at 450 °C in Table 4, which are labeled as LC-P-Mo<sub>2</sub>C.

As seen in Table 4, LC-P-Mo<sub>2</sub>C is even more active than our original P-K-Mo<sub>2</sub>C catalyst, indicating the performance of K-Mo<sub>2</sub>C is very sensitive to the carburization conditions. The difference in performance can likely be attributed to the structure of each catalyst, where XRD and XPS in Fig. S18 and S19 (ESI†) respectively, show the primary phase of LC-P-Mo<sub>2</sub>C is Mo<sub>2</sub>C with some surface oxides. The bulk structure of the resynthesized LC-P-Mo<sub>2</sub>C, shown by XRD in Fig. S18 (ESI†) is similar to that of L-K-Mo<sub>2</sub>C, but the XPS in Fig. S19 (ESI†) shows distinctly more surface carbide and less MoO<sub>3</sub> in LC-P-Mo<sub>2</sub>C versus L-K-Mo<sub>2</sub>C. Together, these data further suggest that an oxycarbide is the active phase for RWGS, agreeing with previous studies over Mo<sub>2</sub>C-based catalysts.<sup>30,41</sup>

There is also a higher potassium to carbon ratio in P-K-Mo<sub>2</sub>C/γ-Al<sub>2</sub>O<sub>3</sub> when compared to L-K-Mo<sub>2</sub>C/γ-Al<sub>2</sub>O<sub>3</sub>, as observed in the C 1s XPS spectra in Fig. 11, although the precursor ratios are kept the same during synthesis of the laboratory and pilot-scale catalysts. As observed in Fig. S19 of the ESI,† the C 1s XPS signal of LC-P-Mo<sub>2</sub>C is much weaker than that of P-K-Mo<sub>2</sub>C, with similar potassium to carbon ratios as P-K-Mo<sub>2</sub>C. However, as mentioned previously, this may be due to an Mo<sub>2</sub>C phase segregating to the surface of LC-P-Mo<sub>2</sub>C during recarburization.

The slight differences between the laboratory and pilot-scale catalysts translate to a measurable difference in catalytic performance, illustrated by the ~25% higher CO STY of the

pilot-scale catalyst at 450 °C and a GHSV of 36.7 L kg<sup>-1</sup> s<sup>-1</sup> in Table 4. Arrhenius experiments on both catalysts also agree with these findings, showing apparent activation energies of 16.3 kcal mol<sup>-1</sup> and 22.5 kcal mol<sup>-1</sup> for P-K-Mo<sub>2</sub>C and L-K-Mo<sub>2</sub>C, respectively. The Arrhenius plot can be found in Fig. S20 of the ESI.†

In fact, the performance of P-K-Mo<sub>2</sub>C/γ-Al<sub>2</sub>O<sub>3</sub> for RWGS at 450 °C in Fig. 1 outperforms all other RWGS catalysts reported in literature under similar conditions when accounting for the cost and production rate of CO. Additionally, benchmarks are included for Cu-ZnO/Al<sub>2</sub>O<sub>3</sub> and FeCrO<sub>x</sub>, the low and high temperature water–gas shift (WGS) catalysts, respectively. When accounting for CO yield and cost of the active phases of the catalysts, it is clear that K-Mo<sub>2</sub>C/γ-Al<sub>2</sub>O<sub>3</sub> has industrial viability for the RWGS reaction, especially at 450 °C.

However, the Fe and Cu catalysts supported on CeO<sub>2</sub> in Fig. 1 and Table 4 perform better than P-K-Mo<sub>2</sub>C/γ-Al<sub>2</sub>O<sub>3</sub> according to certain metrics (\$ metal kg CO<sup>-1</sup>). It is important to note that the high performance of these transition metal catalysts are partially from the higher H<sub>2</sub>:CO<sub>2</sub> ratio (4:1), which results in an equilibrium conversion at 400 °C of 41.3% versus 36.7% for a 3:1 H<sub>2</sub>:CO<sub>2</sub> ratio.<sup>25,34,60</sup> These studies by Dai *et al.* are also performed at atmospheric pressure, which provides proof-of-concept for catalytic activity and selectivity, however, it is also necessary to operate catalysts at more relevant industrial conditions to examine the catalyst scalability.<sup>61</sup> For P-K-Mo<sub>2</sub>C, we have included measurements at atmospheric pressure (0.1 MPa) as references in Fig. 1 and Table 4, which result in lower conversion and CO selectivity than the analogous experiment at high pressure (2.1 MPa).

Although P-K-Mo<sub>2</sub>C/γ-Al<sub>2</sub>O<sub>3</sub> is a high-performance catalyst at 450 °C, at 600 °C the CO selectivity rapidly declines with time-on-stream, as detailed in Fig. 5. The catalyst after the time-on-stream trial at 600 °C was collected, reduced and run under analogous reaction conditions and noted in Table 4 as “Revitalized”. Within this trial, the CO selectivity did not recover to the initial value during the first 14 h on-stream in Fig. 5. Additionally, the XRD patterns collected after RWGS at 300 °C and 600 °C in Fig. 3 suggest that the bulk structure of the catalyst is unchanged at both temperatures, but the significant decrease in CO selectivity suggests the active phase of the catalyst is transient at 600 °C.

From the XPS data and chemisorption data of CO<sub>2</sub> and CO after reaction at 600 °C, the catalytic surface likely becomes coked and oxidized. The coking is evidenced by the high C 1s counts at 600 °C relative to the catalyst reacted at lower temperatures. Oxidation of the surface can be inferred by the decrease in CO<sub>2</sub> adsorption and corresponding increase in CO adsorption after reaction at 600 °C (Table 3), when combined with the DFT calculations, which show that oxygen-modified Mo<sub>2</sub>C binds CO much more strongly than CO<sub>2</sub> (Fig. 8).

Furthermore, additional DFT calculations of CO and CO<sub>2</sub> binding at higher coverage (Fig. 9) indicate that oxygen coverage likely does not exceed 0.75 ML, since both CO and CO<sub>2</sub> binding is endothermic at high coverage, while experiments show that the catalyst remains active. Moreover, our calculations demonstrate that CO consistently binds more strongly than CO<sub>2</sub> at oxygen coverage up to and including 0.75 ML on the Mo-terminated surface. Calculations on the C-terminated Mo<sub>2</sub>C, found in Fig. S14 of the ESI,† indicate that neither CO nor CO<sub>2</sub> adsorb.

Together, these data suggest that coking and oxidation of the catalytic surface cause weaker binding of CO<sub>2</sub> relative to CO, resulting in higher surface coverage of CO and subsequent hydrogenation to CH<sub>4</sub>, the undesired product. As an alternative mechanism, the coke accumulating on the catalyst surface could be subsequently hydrogenated to CH<sub>4</sub>, similar to processes used to remove coke from the surface of catalysts during carburization.<sup>62</sup>

An increase in CH<sub>4</sub> selectivity is also observed during the recycle experiments at higher recycle ratios in Fig. 7. When evaluating the scale-up viability of K-Mo<sub>2</sub>C/γ-Al<sub>2</sub>O<sub>3</sub>, it is important to assess if the increase in CO yield at higher recycle ratios is worth the expense of decreased CO selectivity. If the desired products are C<sub>6+</sub> hydrocarbons, then every mole of CH<sub>4</sub> produced within the RWGS reactor is a waste of energy and valuable H<sub>2</sub>. Depending on the exact application of the catalyst and process, it is possible a more moderate recycle ratio of 1 is desired, which results in a CO<sub>2</sub> conversion of 71% with a CO selectivity approaching 95%. This result is arguably better than the single pass conversion of 48.1% with a CO selectivity of 98.2%, because in a two-reactor CO<sub>2</sub>-FT process, unreacted CO<sub>2</sub> will likely be hydrogenated to methane in the downstream FT reactor.<sup>63</sup> Nevertheless, the performance of K-Mo<sub>2</sub>C/γ-Al<sub>2</sub>O<sub>3</sub> at 450 °C is arguably better than any other catalyst tested under similar conditions. With the low-cost of Mo, K and Al<sub>2</sub>O<sub>3</sub>, the

industrial viability is clear, and K-Mo<sub>2</sub>C/γ-Al<sub>2</sub>O<sub>3</sub> should be further tested and explored for scale-up.

### Industrial deployment

The first step of industrial scale conversion of CO<sub>2</sub> is sourcing CO<sub>2</sub> either directly from effluent flue gases or through atmospheric carbon capture processes.<sup>9</sup> Depending on the CO<sub>2</sub> and H<sub>2</sub> source, industrial CO<sub>2</sub> utilization can have significant impacts on the chemical and energy supply chains.<sup>64</sup> To compare the cost associated with different types of CO<sub>2</sub> utilization technologies, the price equivalent of converted CO<sub>2</sub> to one gallon of gasoline (gge) is a useful metric.

One study by Stechel *et al.* indicates that the cost of using CO<sub>2</sub> via flue gas or direct air capture would contribute \$0.35 gge<sup>-1</sup> to \$5.34 gge<sup>-1</sup>, without accounting for the cost of hydrogen.<sup>65</sup> The estimated cost of production for a gallon of liquid fuel from CO<sub>2</sub> and H<sub>2</sub> is \$4.14 gge<sup>-1</sup>,<sup>66</sup> not including estimated capture costs, bringing a combined fuel cost potentially as high as \$9.48 gge<sup>-1</sup>, far from a cost-competitive price when compared to traditional petrochemical production.

These rough estimates on the feasibility of CO<sub>2</sub> utilization can give some insight into the overall economic feasibility of the process, showing that advancements in lowering the cost of CO<sub>2</sub> and H<sub>2</sub> are both necessary. However, determination of inherent scalability is imperative for effective catalytic development and can be researched in parallel to improved carbon capture and H<sub>2</sub> production technologies.<sup>73–75</sup>

As such, there is a need to benchmark the performance of RWGS catalysts and determine suitability for incorporation into a CO<sub>2</sub> utilization process.<sup>67–71</sup> The authors have proposed two metrics to directly compare and evaluate different catalysts for scale-up. These metrics are CO production rate (kg CO kg metal<sup>-1</sup> day<sup>-1</sup>) and material cost of CO (\$ metal kg CO<sup>-1</sup>). The current work shows that P-K-Mo<sub>2</sub>C/γ-Al<sub>2</sub>O<sub>3</sub> is a top performing catalyst for both of the above metrics (found closest to the top right of Fig. 1), indicating that P-K-Mo<sub>2</sub>C meets the challenge of developing a highly stable RWGS catalyst with high CO selectivity that translates to the pilot-scale.<sup>72</sup> With further development of CO<sub>2</sub> capture technologies,<sup>76</sup> CO<sub>2</sub> utilization could become an environmentally friendly and economically competitive process compared to traditional liquid fuel production.

Although not yet economically competitive with fossil-fuel sourced hydrocarbon production, US Naval Research Laboratory (NRL) is developing a proof of concept system capable of producing up to four liters of liquid hydrocarbon fuel per day from seawater as part of a project to provide fuel for the Navy at sea. The overall system consists of three modular skids: (1) an electrolytic cation exchange module (E-CEM), which can process 135 000 L of seawater per day (94 L min<sup>-1</sup>) to produce 21 000 L of H<sub>2</sub> (14.5 L min<sup>-1</sup>) and 7000 L of CO<sub>2</sub> (4.9 L min<sup>-1</sup>); (2) a gas collection and storage skid, to dry, compress and store the H<sub>2</sub> and CO<sub>2</sub> produced by the E-CEM; and (3) a fuel synthesis skid, containing RWGS and FT reactors.<sup>77–79</sup> The design of each skid and a general process flow diagram for the system can be found in Fig. 13. After demonstrating the viability of P-K-Mo<sub>2</sub>C for pilot-scale RWGS, the next step is to integrate the three



**Fig. 13** NRL modular seawater-to-fuel system consisting of an electrolytic cation exchange module (E-CEM), gas collection and storage skid and fuel synthesis skid. The pilot-scale system can produce up to four liters of jet fuel per day ( $2.8 \text{ mL min}^{-1}$ ).

modules together and demonstrate proof of concept for the overall seawater-to-fuel system. Although the capacity of the system is an insignificant fraction of the total fuel usage of the US Department of Defense (48 million L day<sup>-1</sup>), the development of the modular system is an important step toward deployment at an industrially relevant scale.<sup>80</sup>

There are also future plans to capture and convert effluent CO<sub>2</sub> from power plants, a research and development goal of the US Department of Energy.<sup>81</sup> Extending P-K-Mo<sub>2</sub>C from CO<sub>2</sub> derived from seawater to CO<sub>2</sub> captured from flue gas of coal fired power plants requires that the stability of P-K-Mo<sub>2</sub>C is tested when exposed to common contaminants such as mercury, sulfur, cadmium and chlorine.<sup>82,83</sup> The overall industrial utility of P-K-Mo<sub>2</sub>C as a RWGS catalyst will ultimately depend if the high stability under pure CO<sub>2</sub> and H<sub>2</sub> can be extended to an inlet gas stream containing traces of contaminants that are the subject of future studies.

Perhaps the most promising aspect of the P-K-Mo<sub>2</sub>C catalyst is the high CO STY at industrially relevant pressures (~2 MPa). There is a need for more RWGS studies over low-cost transition metal catalysts under industrially relevant conditions.<sup>61</sup> In the current work, we have addressed this need, and as shown in Fig. 1 and Table 4, the overall performance of K-Mo<sub>2</sub>C and cost of CO at 450 °C is unmatched by the current state-of-the-art. Operating the catalyst at elevated pressures allows the effluent gas from the RWGS reactor to be fed directly into a downstream FT or methanol synthesis reactor. The challenge of FT is that unreacted CO<sub>2</sub> after RWGS can be converted into undesirable CH<sub>4</sub> over typical FT catalysts.<sup>16</sup> With a recycle stream and further process optimization, we can react the majority of CO<sub>2</sub> under milder conditions when compared to the very high temperatures (~800 °C) required for full conversion.

Another option is to integrate the RWGS catalyst with a FT active phase for a CO<sub>2</sub>-FT tandem catalyst. Although such tandem catalysts are difficult to design, the distinct advantages of operating CO<sub>2</sub>-FT over a tandem catalyst or dual-bed configuration are: (1) CO<sub>2</sub>-FT is an exothermic reaction, and as a result, the heat evolved from FT can be used to supply energy to the endothermic RWGS, increasing the thermal efficiency of the overall process above the ~38% for stand-alone RWGS;<sup>8,84</sup> and (2) higher CO<sub>2</sub> conversion can be achieved by using a sufficiently fast FT catalyst to rapidly consume CO to drive the reaction equilibrium toward hydrocarbon products *via* Le'Chatelier's principle. Overcoming equilibrium limitations

of thermally-driven CO<sub>2</sub> hydrogenation reactions without recycling unconverted species has been recognized as a significant challenge for industrial deployment.<sup>85</sup> However, as we have shown here, the P-K-Mo<sub>2</sub>C catalyst is stable and produces CO with high selectivity up to a recycle ratio of two.

If methanol is desired as a final product instead of CO, it may not be necessary to run RWGS with multi-pass conversion, increasing the utility of our P-K-Mo<sub>2</sub>C catalyst. Under the pilot-scale operating conditions with recycle in Fig. 7, the effluent CO:CO<sub>2</sub> ratio is ~0.8 with a stoichiometric number of  $M = 2$  ( $M = \frac{M_{\text{H}_2} - M_{\text{CO}_2}}{M_{\text{CO}} + M_{\text{CO}_2}}$ ).<sup>86,87</sup> Upon the addition of additional H<sub>2</sub> (1 mol per mol of effluent CO) the effluent gas composition can be brought within the typical range for methanol synthesis.<sup>88</sup> Additionally, because we are running the RWGS reaction under higher pressures (2.1 MPa), after water and heat removal, the effluent from our pilot reactor requires less pressurization for downstream methanol synthesis ( $P = 5\text{--}15 \text{ MPa}$ ) relative to other RWGS studies (0.1 MPa).

Industrial deployment of the RWGS reaction as part of a cyclical economy to utilize CO<sub>2</sub> as a carbon source for the above examples requires a source of renewable and CO<sub>2</sub>-free H<sub>2</sub>. Currently, the vast majority (*ca.* 90%) of H<sub>2</sub> is produced from either steam reforming of CH<sub>4</sub> or coal gasification, resulting in significant CO<sub>2</sub> emissions.<sup>14</sup> For industrial viability, and to produce fuel that is cost competitive with gasoline, estimates show that the cost of renewable H<sub>2</sub> must be reduced to between \$2.60 to \$3.00 kg<sup>-1</sup>.<sup>89,90</sup> As mentioned above, NRL has developed a process for co-generation of H<sub>2</sub> and CO<sub>2</sub> from seawater, which if deployed on a large enough scale, can also mitigate the negative effects associated with ocean acidification that cannot be resolved by direct air capture.<sup>91</sup>

## Conclusions

K-Mo<sub>2</sub>C/γ-Al<sub>2</sub>O<sub>3</sub> is a highly active, selective and stable RWGS catalyst at both the laboratory and pilot-scale within the temperature range of 300 to 450 °C. However, at the highest temperature tested of 600 °C, the CO selectivity significantly decreases due to coking and oxidation of the Mo-based active phase of K-Mo<sub>2</sub>C/γ-Al<sub>2</sub>O<sub>3</sub>. This is evidenced by Mo 3d, C 1s and O 1s XPS data, DFT calculations of CO<sub>2</sub> and CO adsorption over Mo<sub>2</sub>C and observed decreases in the catalytically active surface

area and CO<sub>2</sub> binding strength, *via* CO<sub>2</sub> pulse chemisorption and CO<sub>2</sub>-TPD, respectively. This work demonstrates K-Mo<sub>2</sub>C/ $\gamma$ -Al<sub>2</sub>O<sub>3</sub> is an effective RWGS catalyst between 300–450 °C at a range of GHSVs, outperforming all other RWGS catalysts reported in literature when accounting for space-time yield of CO and cost of the active phase. Therefore, K-Mo<sub>2</sub>C/ $\gamma$ -Al<sub>2</sub>O<sub>3</sub> is viable for scale-up as part of a large-scale process for CO<sub>2</sub> hydrogenation to value-added chemicals and fuels.

## Authors contribution

MJ prepared the manuscript and performed the laboratory-scale experiments with help from MV. JH and LF supervised and conducted the pilot-scale experiments. DB and MD performed the DFT calculations and GM supervised the computational tasks of the project. JM and JB facilitated analysis and communication of the data. HW supervised the design, planning and execution of the experiments at NRL. MP conceptualized and coordinated the work and supervised the design, planning and execution of the experiments at the University of Rochester.

## Conflicts of interest

There are no conflicts to declare.

## Acknowledgements

We acknowledge support from the US Department of Defense, Office of Naval Research, under Award No. N00173-18-P-1439. This research used the 8-ID beamline (ISS) of the National Synchrotron Light Source II, a US Department of Energy (DOE) Office of Science User Facility operated for the DOE Office of Science by Brookhaven National Laboratory under Contract No. DE-SC0012704. DB, MD and GM would like to acknowledge computational support from the Center for Research Computing at the University of Pittsburgh.

## References

- Saeidi, S., Najari, F., Fazlollahi, M. K., Nikoo, F., Sefidkon, J. J., Klemeš, L. L., Baxter, *Renewable Sustainable Energy Rev.*, 2017, **80**, 1292–1311.
- Ma, N., Sun, X., Zhang, N., Zhao, F., Xiao, W., Wei and Y. Sun, *Catal. Today*, 2009, **148**, 221–231.
- Zhang, K.-W., Jun, K.-S., Ha, Y.-J., Lee and S. C. Kang, *Environ. Sci. Technol.*, 2014, **48**, 8251–8257.
- Graves, S. D., Ebbesen, M., Mogensen and K. S. Lackner, *Renewable Sustainable Energy Rev.*, 2011, **15**, 1–23.
- Saeidi, N. A. S., Amin and M. R. Rahimpour, *J. CO<sub>2</sub> Util.*, 2014, **5**, 66–81.
- Peter, S. C., *ACS Energy Lett.*, 2018, **3**, 1557–1561.
- Sanz-Pérez, E. S., Murdock, C. R., Didas and C. W. Jones, *Chem. Rev.*, 2016, **116**, 11840–11876.
- Ma, Z. and M. D. Porosoff, *ACS Catal.*, 2019, **9**, 2639–2656.
- Keith, D. W., Holmes, G., St. Angelo and K. Heidel, *Joule*, 2018, **2**, 1573–1594.
- Olah, G. A., Mathew, T., Goeppert and G. K. Surya Prakash, *Top. Catal.*, 2018, **61**, 522–529.
- Choi, Y. H., Jang, Y. J., Park, H., Kim, W. Y., Lee, S. H., Choi and J. S. Lee, *Appl. Catal., B*, 2017, **202**, 605–610.
- Li, W., Wang, H., Jiang, X., Zhu, J., Liu, Z., Guo and C. Song, *RSC Adv.*, 2018, **8**, 7651–7669.
- Wei, J., Ge, Q., Yao, R., Wen, Z., Fang, C., Guo, L., Xu and J. Sun, *Nat. Commun.*, 2017, **8**, 15174.
- Centi, G., Quadrelli and S. Perathoner, *Energy Environ. Sci.*, 2013, **6**, 1711–1731.
- Gnanamani, M. K., Jacobs, G., Hamdeh, H. H., Shafer, F., Liu, S. D., Hopps, G. A., Thomas and B. H. Davis, *ACS Catal.*, 2016, **6**, 913–927.
- Prieto, G., *ChemSusChem*, 2017, **10**, 1056–1070.
- Daza, Y. A. and J. N. Kuhn, *RSC Adv.*, 2016, **6**, 49675–49691.
- Rodriguez, J. A., Liu, P., Wang, X., Wen, W., Hanson, J., Hrbek, M., Pérez and J. Evans, *Catal. Today*, 2009, **143**, 45–50.
- Newsome, D. S., *Catal. Rev.*, 1980, **21**, 275–318.
- Boix, A. V., Ulla, M. A. A. and J. O. Petunchi, *J. Catal.*, 1996, **162**, 239–249.
- Alayoglu, S., Beaumont, K., Zheng, F., Pushkarev, H., Zheng, V., Iablokov, Z., Liu, J., Guo, N., Kruse and G. A. Somorjai, *Top. Catal.*, 2011, **54**, 778.
- Wang, C., Guan, E., Wang, L., Chu, X., Wu, Z., Zhang, Z., Yang, Y., Jiang, L., Zhang, X., Meng, B. C., Gates and F.-S. Xiao, *J. Am. Chem. Soc.*, 2019, **141**, 8482–8488.
- Chen, X., Su, X., Duan, H., Liang, B., Huang, Y., Zhang, T. and Y. Chen, *Catal. Today*, 2017, **281**, 312–318.
- Goguet, A., Meunier, F., Breen, J. P., Burch, R., Petch and A. Faur Ghenciu, *J. Catal.*, 2004, **226**, 382–392.
- Dai, B., Zhou, G., Ge, S., Xie, H., Jiao, Z., Zhang, G., Xiong, K. and C. J. Chem. Eng., 2017, **95**, 634–642.
- Levy, R. B. and M. Boudart, *Science*, 1973, **181**, 547–549.
- Solymosi, F., Oszkó, A., Bánsági and P. Tolmacsov, *J. Phys. Chem. B*, 2002, **106**, 9613–9618.
- Shi, Y., Yang, Y.-W., Li and H. Jiao, *Appl. Catal., A*, 2016, **524**, 223–236.
- Koverga, A. A., Flórez, E., Dorkis and J. A. Rodriguez, *J. Phys. Chem. C*, 2019, **123**, 8871–8883.
- Porosoff, M. D., Yang, X., Boscoboinik and J. G. Chen, *Angew. Chem.*, 2014, **126**, 6823–6827.
- Ledoux, M. J., Huu, C. P., Guille and H. Dunlop, *J. Catal.*, 1992, **134**, 383–398.
- Liu, X., Kunkel, C., Ramírez De La Piscina, P., Hom, F., Viñes and F. Illas, *ACS Catal.*, 2017, **7**, 4323–4335.
- Porosoff, M. D., Kattel, S., Li, W., Liu, P. and J. G. Chen, *Chem. Commun.*, 2015, **51**, 6988–6991.
- Xu, W., Ramírez, P. J., Stacchiola, D., Brito and J. A. Rodriguez, *Catal. Lett.*, 2015, **145**, 1365–1373.
- Posada-Pérez, S., Viñes, P. J., Ramirez, A. B., Vidal, J. A., Rodriguez and F. Illas, *Phys. Chem. Chem. Phys.*, 2014, **16**, 14912–14921.
- Xiang, M., Li, D., Zou, J., Li, W., Sun, Y. and She, X., *J. Nat. Gas Chem.*, 2010, **19**, 151–155.

- 37 W. D. Mross, *Catal. Rev.*, 1983, **25**, 591–637.
- 38 D. Li, N. Ichikuni, S. Shimazu and T. Uematsu, *Appl. Catal., A*, 1998, **172**, 351–358.
- 39 C. L. O'Young, *J. Phys. Chem.*, 1989, **93**, 2016–2018.
- 40 J. R. Morse, M. Juneau, J. W. Baldwin, M. D. Porosoff and H. D. Willauer, *J. CO<sub>2</sub> Util.*, 2020, **35**, 38–46.
- 41 M. D. Porosoff, J. W. Baldwin, X. Peng, G. Mpourmpakis and H. D. Willauer, *ChemSusChem*, 2017, **10**, 2408–2415.
- 42 M. E. Dry, *J. Mol. Catal.*, 1982, **17**, 133–144.
- 43 J. Xu, Y. Yang and Y.-W. Li, *Curr. Opin. Chem. Eng.*, 2013, **2**, 354–362.
- 44 G. Kresse and J. Furthmüller, *Comput. Mater. Sci.*, 1996, **6**, 15–50.
- 45 M. Dixit, X. Peng, M. D. Porosoff, H. D. Willauer and G. Mpourmpakis, *Catal. Sci. Technol.*, 2017, **7**, 5521–5529.
- 46 M. D. Porosoff, J. W. Baldwin, X. Peng, G. Mpourmpakis and H. D. Willauer, *ChemSusChem*, 2017, **10**, 2408–2415.
- 47 J. P. Perdew, K. Burke and M. Ernzerhof, *Phys. Rev. Lett.*, 1996, **77**, 3865.
- 48 M. Methfessel and A. Paxton, *Phys. Rev. B: Condens. Matter Mater. Phys.*, 1989, **40**, 3616.
- 49 E. Parthé and V. Sadogopan, *Acta Crystallogr.*, 1963, **16**, 202–205.
- 50 A. M. Karim, C. Howard, B. Roberts, L. Kovarik, L. Zhang, D. L. King and Y. Wang, *ACS Catal.*, 2012, **2**, 2387–2394.
- 51 M. Newville, *J. Synchrotron Radiat.*, 2001, **8**, 322–324.
- 52 B. Ravel and M. Newville, *J. Synchrotron Radiat.*, 2005, **12**, 537–541.
- 53 M. D. Porosoff and J. G. Chen, *J. Catal.*, 2013, **301**, 30–37.
- 54 P. Liu and J. A. Rodriguez, *J. Phys. Chem. B*, 2006, **110**, 19418–19425.
- 55 M. Dixit, X. Peng, M. D. Porosoff, H. D. Willauer and G. Mpourmpakis, *Catal. Sci. Technol.*, 2017, **7**, 5521–5529.
- 56 K. Oshikawa, M. Nagai and S. Omi, *J. Phys. Chem. B*, 2001, **105**, 9124–9131.
- 57 S. Selvakumar, N. Nuns, M. Trentesaux, V. S. Batra, J. M. Giraudon and J. F. Lamonier, *Appl. Catal., B*, 2018, **223**, 192–200.
- 58 P. Delporte, F. D. R. Meunier, C. Pham-Huu, P. Vennegues, M. J. Ledoux and J. Guille, *Catal. Today*, 1995, **23**, 251–267.
- 59 J. G. Choi and L. T. Thompson, *Appl. Surf. Sci.*, 1996, **93**, 143–149.
- 60 A. Bansode, B. Tidona, P. R. von Rohr and A. Urakawa, *Catal. Sci. Technol.*, 2013, **3**, 767–778.
- 61 E. Schwab, A. Milanov, S. A. Schunk, A. Behrens and N. Schödel, *Chem. Ing. Tech.*, 2015, **87**, 347–353.
- 62 Y. C. Kimmel, D. V. Esposito, R. W. Birkmire and J. G. Chen, *Int. J. Hydrogen Energy*, 2012, **37**, 3019–3024.
- 63 Y. Zhang, G. Jacobs, D. E. Sparks, M. E. Dry and B. H. Davis, *Catal. Today*, 2002, **71**, 411–418.
- 64 C. Ampelli, S. Perathoner and G. Centi, *Philos. Trans. R. Soc., A*, 2015, **373**, 20140177.
- 65 E. B. Stechel and J. E. Miller, *J. CO<sub>2</sub> Util.*, 2013, **1**, 28–36.
- 66 A. Elgowainy, J. Han, J. Ward, F. Joseck, D. Gohlke, A. Lindauer, T. Ramsden, M. Biddy, M. Alexander, S. Barnhart, I. Sutherland, L. Verduzco and T. Wallington, Cradle-to-Grave Lifecycle Analysis of U.S. Light Duty Vehicle-Fuel Pathways: A Greenhouse Gas Emissions and Economic Assessment of Current (2015) and Future (2025–2030) Technologies, United States, 2016.
- 67 M. Aresta, A. Dibenedetto and A. Angelini, *J. CO<sub>2</sub> Util.*, 2013, **3–4**, 65–73.
- 68 E. Alper and O. Yuksel Orhan, *Petroleum*, 2017, **3**, 109–126.
- 69 F. D. Meylan, V. Moreau and S. Erkman, *J. CO<sub>2</sub> Util.*, 2015, **12**, 101–108.
- 70 M. R. Hamilton, H. J. Herzog and J. E. Parsons, *Energy Procedia*, 2009, **1**, 4487–4494.
- 71 K. Roh, H. Lim, W. Chung, J. Oh, H. Yoo, A. S. Al-Hunaidy, H. Imran and J. H. Lee, *J. CO<sub>2</sub> Util.*, 2018, **26**, 60–69.
- 72 X. Su, X. Yang, B. Zhao and Y. Huang, *J. Energy Chem.*, 2017, **26**, 854–867.
- 73 J. Rostrup-Nielsen, *J. Mol. Catal. A: Chem.*, 2000, **163**, 157–162.
- 74 S. Mitchell, N.-L. Michels and J. Pérez-Ramírez, *Chem. Soc. Rev.*, 2013, **42**, 6094–6112.
- 75 M. Campanati, G. Fornasari and A. Vaccari, *Catal. Today*, 2003, **77**, 299–314.
- 76 P. Vibhatavata, J.-M. Borgard, M. Tabarant, D. Bianchi and C. Mansilla, *Int. J. Hydrogen Energy*, 2013, **38**, 6397–6405.
- 77 F. DiMascio, D. R. Hardy, M. K. Lewis, H. D. Willauer and F. Williams, *US Pat.*, 9303323, U.S. Patent and Trademark Office, Washington, DC, 2016.
- 78 F. DiMascio, H. D. Willauer, D. R. Hardy, F. Williams and M. K. Lewis, *US Pat.*, 9719178, U.S. Patent and Trademark Office, Washington, DC, 2017.
- 79 F. DiMascio, H. D. Willauer, D. R. Hardy, F. Williams and M. K. Lewis, *US Pat.*, 10450661, U.S. Patent and Trademark Office, Washington, DC, 2019.
- 80 R. W. Dorner, D. R. Hardy, F. W. Williams and H. D. Willauer, *Energy Environ. Sci.*, 2010, **3**, 884.
- 81 U. S. DOE, U.S. Department of Energy Announces \$110M for Carbon Capture, Utilization, and Storage, <https://www.energy.gov/articles/us-department-energy-announces-110m-carbon-capture-utilization-and-storage>, (accessed 4/19/2020, 2020).
- 82 C. E. Billings and W. R. Matson, *Science*, 1972, **176**, 1232–1233.
- 83 O. I. Joensuu, *Science*, 1971, **172**, 1027–1028.
- 84 D. S. Mallapragada, N. R. Singh, V. Curteanu and R. Agrawal, *Ind. Eng. Chem. Res.*, 2013, **52**, 5136–5144.
- 85 R. G. Grim, Z. Huang, M. T. Guarneri, J. R. Ferrell, L. Tao and J. A. Schaidle, *Energy Environ. Sci.*, 2020, **13**, 472–494.
- 86 G. Liu, D. Willcox, M. Garland and H. H. Kung, *J. Catal.*, 1984, **90**, 139–146.
- 87 D. Milani, R. Khalilpour, G. Zahedi and A. Abbas, *J. CO<sub>2</sub> Util.*, 2015, **10**, 12–22.
- 88 S. S. Iyer, T. Renganathan, S. Pushpavanam, M. Vasudeva Kumar and N. Kaisare, *J. CO<sub>2</sub> Util.*, 2015, **10**, 95–104.
- 89 Q. Smejkal, U. Rodemerck, E. Wagner and M. Baerns, *Chem. Ing. Tech.*, 2014, **86**, 679–686.
- 90 G. Centi and S. Perathoner, in *Green Carbon Dioxide*, ed. G. Centi and S. Perathoner, 2014, pp. 1–24, DOI: 10.1002/9781118831922.ch1.
- 91 S. Mathesius, M. Hofmann, K. Caldeira and H. J. Schellnhuber, *Nat. Clim. Change*, 2015, **5**, 1107–1113.
- 92 P. Chen, G. Zhao, X.-R. Shi, J. Zhu, J. Ding and Y. Lu, *iScience*, 2019, **17**, 315–324.
- 93 M. R. Gogate and R. J. Davis, *Catal. Commun.*, 2010, **11**, 901–906.